

Department of Technical Physics  
Faculty of Information Technology  
Helsinki University of Technology  
02150 Espoo, Finland

# ACOUSTIC AND OPTICAL INVESTIGATIONS OF SUPERFLUID $^3\text{He}$

Antti Manninen

Low Temperature Laboratory

Dissertation for the degree of Doctor of Technology  
to be presented with due permission for public  
examination and debate in Auditorium F1 at  
Helsinki University of Technology (Espoo, Finland)  
on the 15th of June, 1993, at 12 noon.

Espoo 1993



# Contents

<b>1. Introduction</b>	<b>1</b>
1.1. Superfluidity of $^3\text{He}$	1
1.2. Superfluid in rotation: vortices	4
1.3. Propagation of ultrasound in $^3\text{He}$	6
1.3.1. Anisotropic sound propagation in $^3\text{He-A}$	7
1.3.2. Collective modes in $^3\text{He-B}$	8
1.3.3. Nonlinear acoustics	10
<b>2. Acoustic experiments</b>	<b>12</b>
2.1. Experimental techniques	12
2.2. Investigations of $^3\text{He-A}$	15
2.2.1. Re-entrant normal flapping mode	15
2.2.2. Rotating $^3\text{He-A}$ in low magnetic fields: vortex transition	17
2.2.3. Rotating $^3\text{He-A}$ in high magnetic fields	20
2.3. Linear acoustics in $^3\text{He-B}$	22
2.3.1. Rotation response in high magnetic fields	22
2.3.2. Anomalous magnetic field dependence of ultrasound attenuation	23
2.3.3. Real squashing mode under rotation	25
2.4. Nonlinear acoustics in $^3\text{He-B}$	27
2.4.1. Observation of two-phonon absorption by the real squashing mode	27
2.4.2. Application of two-phonon absorption: dispersion in the rsq-mode	30
2.4.3. Two-phonon pair-breaking edge	31
<b>3. Optical experiments</b>	<b>33</b>
3.1. Experimental techniques	33
3.1.1. Preliminary tests of optics at low temperatures	33
3.1.2. Optical apparatus in ROTA2	36
3.2. Experimental results	40
3.2.1. Superfluid transition	40
3.2.2. Parabolic surface profile under rotation	42
3.2.3. Fountain effect	45
3.3. Future directions	47
<b>4. Summary</b>	<b>48</b>
<b>5. Publications</b>	<b>50</b>
<b>Acknowledgements</b>	<b>54</b>
<b>References</b>	<b>55</b>



# 1. Introduction

This thesis is an experimental survey of properties of rotating and stationary superfluid  $^3\text{He}$ . Two techniques, acoustics and optics, were used.

Ultrasound, together with NMR, has provided most of the present experimental knowledge about the superfluid phases of  $^3\text{He}$ . We applied acoustics for the first time to study rotating  $^3\text{He}$  [P2, P4 – P6]. The main result was the discovery of a new vortex in  $^3\text{He-A}$  when the magnetic field is low. New phenomena were observed in stationary  $^3\text{He}$  as well [P1, P3, P4, P7 – P9]. Most importantly, one of the collective modes, the real squashing (rsq) mode, of  $^3\text{He-B}$  could be excited by means of two-phonon absorption.

Superfluid  $^3\text{He}$  was studied optically for the first time. No one has previously *seen*  $^3\text{He}$  in the superfluid state. The principal achievement was developing techniques which facilitate optical experiments at temperatures below 1 mK, required to study superfluid  $^3\text{He}$ . Optical fibers were used to transmit light between room temperature and the cold parts of the cryostat [P10, P11]. Before these investigations, photography had not been done below 10 mK. The usefulness of optics as a probe of the superfluid phases of  $^3\text{He}$  was demonstrated by studying the macroscopic shape of the free surface of rotating  $^3\text{He-B}$ . The classical parabolic meniscus was observed, which is indicative of the equilibrium density of vortices.

## 1.1. Superfluidity of $^3\text{He}$

At low temperatures, quantum-mechanical effects are of crucial importance in determining the properties of condensed helium. Already the fact that helium remains liquid – a quantum liquid – down to the lowest temperatures is a consequence of the large quantum-mechanical zero-point motion of the light, inert helium atoms. The attractive van der Waals interaction between the atoms is weaker than the zero-point energy. Consequently, helium does not solidify unless the atoms are forced close together by an externally applied pressure of about 30 bars [1].

The two stable isotopes of helium,  $^3\text{He}$  and  $^4\text{He}$ , have strikingly different macroscopic properties at low temperatures. This follows from their different quantum statistics:  $^3\text{He}$ -atoms are fermions, while  $^4\text{He}$ -atoms are bosons. At the "lambda" temperature  $T_\lambda = 2.17\text{ K}$  (s.v.p.), liquid  $^4\text{He}$  undergoes a phase transition into the superfluid state, in which the frictionless flow of a macroscopic number of particles is possible. This phase change is closely connected with the Bose-Einstein condensation of an ideal boson gas, during which the population of the ground state becomes macroscopic [2].

Such a condensation in a fermion system seems impossible, at first sight, because of the Pauli exclusion principle.  $^3\text{He}$  behaves, indeed, as a "normal" liquid down to temperatures three orders of magnitude below  $T_\lambda$ . Between  $T \simeq 3\text{ mK}$  and  $T \simeq 100\text{ mK}$  the properties of liquid  $^3\text{He}$  are well described by Landau's theory for normal Fermi liquids [3]. However, Nature has arranged a trick: two  $^3\text{He}$ -atoms can form a so-called Cooper pair, which behaves effectively as a boson and becomes Bose-condensed. This is the heart of the BCS-theory [4], which was first developed to explain the superconductivity of electrons, observed in many metals at low temperatures. Superfluid  $^3\text{He}$  was discovered in 1972, at  $T < 3\text{ mK}$  [5]. Two different phase transitions were observed, corresponding to two superfluid phases in zero

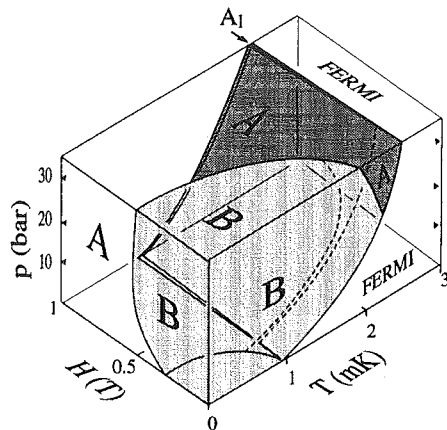


**Figure 1.** The  $p$ - $T$ - $H$  phase diagram of liquid  $^3\text{He}$  at low temperatures. The Fermi-liquid region and the superfluid A-, B-, and  $A_1$ -phases are marked.

magnetic field,  $^3\text{He}$ -A and  $^3\text{He}$ -B. The low-temperature phase diagram of  $^3\text{He}$  is presented in Fig. 1.

At finite temperatures a superfluid with density  $\rho$  can be phenomenologically considered as a mixture of two interpenetrating components: the normal component with density  $\rho_n$  behaves as a classical liquid, while the condensate of density  $\rho_s = \rho - \rho_n$  displays the superfluid properties [2]. At the zero-temperature limit  $\rho_n \rightarrow 0$ , whereas  $\rho_s$  approaches zero near the superfluid transition temperature  $T_c$ . For anisotropic superfluids, like  $^3\text{He}$ -A,  $\rho_n$  and  $\rho_s$  are tensor quantities.

The properties of the superfluid component are governed by the order parameter, which describes the macroscopic wave function of the condensate. The order parameter for superfluid  $^4\text{He}$  is a complex scalar quantity that can be presented in the form

$$\psi(\mathbf{r}) = |\psi(\mathbf{r})|e^{i\phi(\mathbf{r})}, \quad (1)$$

where  $|\psi(\mathbf{r})| = \sqrt{\rho_s(\mathbf{r})/m_4}$ , with  $m_4$  the mass of a  $^4\text{He}$ -atom, and  $\phi(\mathbf{r})$  is a real-valued phase factor. In conventional superconductors, where the Cooper pairs are formed by electrons having opposite spins, the order parameter is a complex scalar as well. The pairs are in the spin-singlet s-wave state with  $S = L = 0$ , where  $S$  is the spin and  $L$  the relative orbital angular momentum of the Cooper pair.

The situation in  $^3\text{He}$  is more complicated: pairing occurs between parallel spins into the spin-triplet ( $S = 1$ ) orbital p-wave ( $L = 1$ ) state, whence the order parameter is a complex-valued  $3 \times 3$  second-rank tensor  $A_{\mu j}$ , with 18 independent real parameters [6]. The indices  $\mu$  and  $j$  in  $A_{\mu j}$  refer to the three spin and the three orbital degrees of freedom, respectively. The complicated structure of the order parameter means that  $^3\text{He}$  is not only a superfluid. It has also many properties of magnets and liquid crystals [7]. Moreover, the existence of several stable superfluid states is possible. In a bulk liquid, three different superfluid phases have been detected:  $^3\text{He}$ -A,  $^3\text{He}$ -B, and  $^3\text{He}$ - $A_1$  (see the phase diagram in Fig. 1). Even more exotic states can exist, for example, inside the vortex-cores of rotating superfluids [8,9].

It is generally accepted that  $^3\text{He-A}$  corresponds to the axial Anderson-Brinkman-Morel (ABM) state [10], with an order parameter

$$A_{\mu j} = \Delta_A(T) \hat{d}_\mu (\hat{m}_j + i \hat{n}_j) ; \quad (2)$$

here  $\hat{\mathbf{d}}$  is a unit vector in spin space, and  $\hat{\mathbf{m}}$  and  $\hat{\mathbf{n}}$  are orthogonal unit vectors in the orbital space, such that  $\hat{\mathbf{l}} = \hat{\mathbf{m}} \times \hat{\mathbf{n}}$  points in the direction of the orbital angular momentum of the Cooper pairs. The energy gap  $\Delta_A(\hat{\mathbf{k}}, T)$  which separates the "normal" quasiparticles from the condensate is given by the magnitude of the order parameter. The gap is anisotropic and has nodes along  $\hat{\mathbf{l}}$ :  $\Delta_A(\hat{\mathbf{k}}, T) = \Delta_A(T) |\sin \theta|$ , where  $\theta$  is the angle between  $\hat{\mathbf{k}}$  and  $\hat{\mathbf{l}}$ . In the weak-coupling approximation  $\Delta_A(0) = 2.03 k_B T_c$ , and  $\Delta_A(T) \rightarrow 3.42 k_B T_c \sqrt{1 - T/T_c}$  when  $T_c$  is approached [6].

There are several interactions which orient the anisotropy axes  $\hat{\mathbf{l}}$  and  $\hat{\mathbf{d}}$  of the A-phase order parameter. Dipole-dipole forces between the nuclear spins of the  $^3\text{He}$ -atoms tend to keep  $\hat{\mathbf{l}}$  and  $\hat{\mathbf{d}}$  parallel or antiparallel. The  $\hat{\mathbf{d}}$ -vector turns perpendicular to an external magnetic field, and  $\hat{\mathbf{l}}$  must be normal to solid walls. The  $\hat{\mathbf{l}}$ -vector has quite an intricate interaction with superflow, as will be discussed in the following Section. Spatial variations in the directions of  $\hat{\mathbf{l}}$  and  $\hat{\mathbf{d}}$  are resisted by the gradient energy. In the presence of several competing interactions, the  $\hat{\mathbf{l}}$ - and  $\hat{\mathbf{d}}$ -vectors form continuous textures in the sample. The length scale for the regions where  $\hat{\mathbf{l}}$  and  $\hat{\mathbf{d}}$  need not be parallel is the dipolar healing length  $\xi_d \simeq 10 \mu\text{m}$ . It is determined by the competition between the dipole-dipole energy and the gradient energy. The corresponding magnetic length  $\xi_H$ , which is the characteristic size of defects where  $\hat{\mathbf{d}}$  and  $\mathbf{H}$  are not perpendicular, is inversely proportional to magnetic field;  $\xi_H = \xi_d$  at the so-called dipolar field  $H_d \simeq 3 \text{ mT}$ .

The B-phase is identified with the Balian-Werthamer (BW) state [11], which has the order parameter

$$A_{\mu j} = \Delta(T) e^{i\phi} R_{\mu j}(\hat{\mathbf{n}}, \theta) \quad (3)$$

in zero magnetic field; here  $\phi$  is a phase factor and  $R_{\mu j}$  a matrix which rotates the spin and orbital coordinates with respect to each other by an angle  $\theta$  about an axis  $\hat{\mathbf{n}}$ . The energy gap  $\Delta(T)$  is isotropic, having a value  $\Delta(0) = 1.764 k_B T_c$  at the zero-temperature limit according to the weak-coupling BCS-theory, and approaching zero as  $3.06 k_B T_c \sqrt{1 - T/T_c}$  near  $T_c$  [6]. However, in strong magnetic fields the energy gap of  $^3\text{He-B}$  becomes anisotropic and is given by [12]

$$|\Delta(\hat{\mathbf{k}})|^2 = \Delta_\perp^2 - (\Delta_\perp^2 - \Delta_\parallel^2)(\hat{\mathbf{k}} \cdot \hat{\mathbf{h}})^2 . \quad (4)$$

The gap  $\Delta_\parallel$  in the direction of the anisotropy axis  $\hat{\mathbf{h}}$  is decreased by the field, and  $\Delta_\perp$  perpendicular to  $\hat{\mathbf{h}}$  is increased. The vector  $\hat{\mathbf{h}}$ , i.e., the direction of effective magnetic field, is related to the applied field  $\mathbf{H}$  as

$$\hat{h}_j = R_{\mu j} H_\mu / H . \quad (5)$$

The spatial variations of the  $\hat{\mathbf{n}}$ -vector, which is affected by several interactions, form a texture in superfluid  $^3\text{He-B}$ . An external magnetic field tends to keep  $\hat{\mathbf{n}} \parallel \mathbf{H}$ . Near solid walls

$\hat{n}$  turns so that the vector  $\hat{n}$  defined in Eq. (5) is perpendicular to the surface. Vortices and the counterflow between the normal and superfluid components can orient the  $\hat{n}$ -vector as well. The healing lengths for the  $\hat{n}$ -texture in  $^3\text{He-B}$  are much longer than those for  $^3\text{He-A}$ ; the magnetic length  $\xi_H \propto 1/H$  is on the order of 1 mm even when  $H = 20$  mT. The dipolar interaction fixes the angle  $\theta$  in Eq. (3) to the value  $\theta_L = \arccos(-1/4) = 104^\circ$ . However, there are some defects, like the  $\theta$ -solitons in spin-mass vortices [13], inside which  $\theta$  deviates from this "magic angle".

## 1.2. Superfluid in rotation: vortices

The velocity of the superfluid component in  $^4\text{He}$  is given by the formula

$$\mathbf{v}_s = \frac{\kappa}{2\pi} \nabla \phi, \quad (6)$$

where  $\kappa = h/m_4 = 9.97 \cdot 10^{-8}$  m<sup>2</sup>/s is the quantum of circulation. This can be derived from the wave function  $\psi(\mathbf{r})$ , Eq. (1), by identifying the quantum-mechanical current density  $\mathbf{j} = (i\hbar/2m_4)(\psi \nabla \psi^* - \psi^* \nabla \psi)$  with  $(\rho_s/m_4)\mathbf{v}_s$  [14]. From Eq. (6) it immediately follows that the velocity field of the superfluid condensate is irrotational:  $\nabla \times \mathbf{v}_s = 0$ . This appears to imply that the superfluid component in a rotating chamber remains at rest. Only the normal component should circulate with the vessel as a solid body, with  $\mathbf{v}_n = \Omega \times \mathbf{r}$  and  $\nabla \times \mathbf{v}_n = 2\Omega$ , where  $\Omega$  is the angular velocity of rotation.

However, Osborne [15] showed experimentally that the superfluid component rotates with the container as well. He studied visually the free surface of rotating superfluid  $^4\text{He}$  and realized that at all temperatures the surface had the classical parabolic profile:

$$z(r) = \Omega^2 r^2 / 2g, \quad (7)$$

where  $z(r)$  is the vertical coordinate of the surface at distance  $r$  from the axis of rotation, and  $g = 9.8$  m/s<sup>2</sup> is the acceleration of gravity. On the other hand, if only the normal component rotates, Eq. (7) should be scaled by the relative amount  $\rho_n/\rho$  of normal liquid:

$$z(r) = (\rho_n/\rho) \Omega^2 r^2 / 2g. \quad (8)$$

At low temperatures, where  $\rho_n/\rho$  is very small, the surface should be almost flat.

This puzzle was solved by Onsager [16] and by Feynman [17], who suggested the existence of vortices: linear defects around which the superfluid component can rotate with velocity field  $v_s(r) \propto r^{-1}$ , for which  $\nabla \times \mathbf{v}_s = 0$  [18]. Single-valuedness of the wave function (1) requires that superflow is quantized: the azimuthal velocity field around the vortices must be

$$v_s(r) = \frac{N\kappa}{2\pi r}, \quad (9)$$

where  $N$  is an integer. Each vortex in rotating  $^4\text{He}$  has a core of atomic size, about 0.1 nm, where  $\rho_s$  vanishes. This prevents the divergence of kinetic energy at  $r = 0$ . In the state of minimum energy, the superfluid component simulates the solid-body rotation of conventional liquids as closely as possible: a regular lattice of singly quantized vortices ( $N = 1$  in Eq. (9)) is formed, with the number density  $n = 2\Omega/\kappa$ . At  $\Omega = 1$  rad/s, the distance between these singu-



larities is about 0.2 mm. The existence of vortices in superfluid  $^4\text{He}$  has been proved most convincingly by Williams and Packard [19]: the vortices were directly photographed, monitoring the electrons that were trapped by the cores.

Quantized vortices are present in rotating superfluid  $^3\text{He}$  as well. This was shown by NMR-experiments in Helsinki [20,21]. The singularities in  $^3\text{He}$  have a much richer structure than in  $^4\text{He}$ . Several types of vortices exist both in  $^3\text{He-A}$  and in  $^3\text{He-B}$ , with phase transitions between them [8,9,12,22,23].

In  $^3\text{He-A}$ , the velocity of the superfluid component cannot be expressed as a simple gradient like in Eq. (6). This means that superflow need not be irrotational. Instead, the Mermin-Ho relation [24]

$$(\nabla \times \mathbf{v}_s)_i = \frac{\kappa}{4\pi} \epsilon_{ijk} \hat{\mathbf{l}} \cdot (\partial_j \hat{\mathbf{l}} \times \partial_k \hat{\mathbf{l}}) \quad (10)$$

is valid. The circulation quantum for superfluid  $^3\text{He}$  is  $\kappa = h/2m_3 = 6.62 \cdot 10^{-8} \text{ m}^2/\text{s}$ , where  $2m_3$  is the mass of a Cooper pair. The superflow field is directly coupled with the  $\hat{\mathbf{l}}$ -texture in an intricate manner. Vortices are formed in rotating bulk  $^3\text{He-A}$ , but their cores can consist of the A-phase. Such continuous structures have been detected in most experiments [9]. It is presently believed that for  $H \gg H_d$  the vortices are of the Seppälä-Volovik type [25], which are doubly quantized. Their schematic  $\hat{\mathbf{l}}$ -texture is shown in Fig. 2a. The size of the "soft core", inside which the  $\hat{\mathbf{d}}$ -vector is orientated perpendicular to the magnetic field but  $\hat{\mathbf{l}}$  deviates from the direction of  $\hat{\mathbf{d}}$ , is on the order of the dipolar length  $\xi_d \approx 10 \mu\text{m}$ . Our observation of a topological transition between two different continuous vortex textures in low magnetic fields [P2] is discussed in Section 2.2.2.

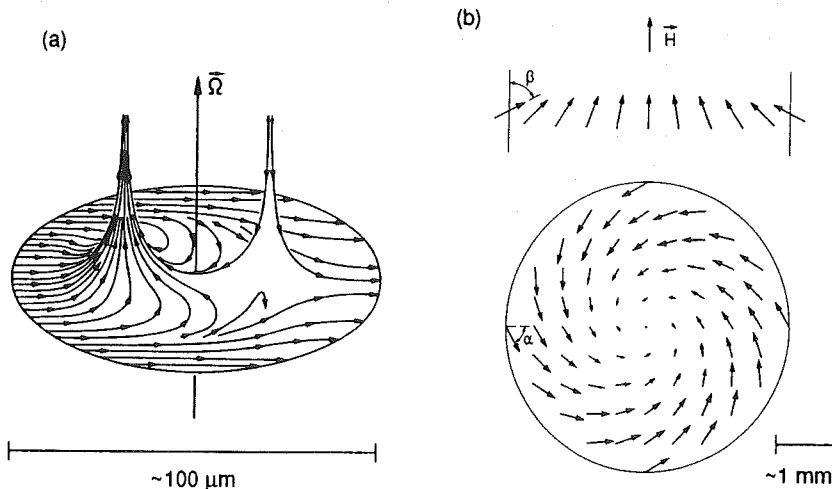


**Figure 2.** (a) The  $\hat{\mathbf{l}}$ -texture of a continuous doubly quantized Seppälä-Volovik vortex in  $^3\text{He-A}$  (from Ref. [26]). (b) The flare-out  $\hat{\mathbf{n}}$ -vector texture for  $^3\text{He-B}$  in an infinite cylinder: side view above and top view below [8,9]. Note the difference in the length scales between (a) and (b).

The existence of singular vortices is possible in  $^3\text{He-A}$ , as well. They have a "hard core" where the order parameter deviates from its bulk form. The core need not be in the normal state; it can rather consist of another superfluid phase. The radius of a singular vortex core in  $^3\text{He-A}$  or in  $^3\text{He-B}$  is on the order of the superfluid coherence length  $\xi \approx 10\text{--}50\text{ nm}$ , i.e., more than two orders of magnitude larger than in  $^4\text{He}$ . For  $H > H_d$  a singular singly quantized vortex with polar phase in the core has the minimum energy among the  $^3\text{He-A}$  vortex types considered theoretically so far [25]. A probable explanation for the absence of singular vortices in most experiments is that the nucleation of continuous vortices is easier. However, in measurements performed with negative ions, two different types of vortices in  $^3\text{He-A}$  were detected [27]. There is some evidence that one of them is singular and the other continuous.

$^3\text{He-B}$  is not less interesting. The order parameter  $A_{\mu j}$  (Eq. (3)), a real quantity multiplied by a phase factor, implies that  $\mathbf{v}_s$  is given by Eq. (6), with  $\kappa = h/2m_3$ . Thus, superflow must be irrotational and, as in  $^4\text{He}$ , only singular vortices are possible. However, the hard cores of vortices in  $^3\text{He-B}$  need not be in the normal state, and several different types of cores are possible [8]. Two of them have been observed experimentally [21], both correspond to singly quantized vortices. For high pressures and temperatures ( $p \gtrsim 18\text{ bar}$ ,  $T \gtrsim 1.5\text{ mK}$ ), the vortex cores are believed to be axisymmetric and consist mainly of  $^3\text{He-A}$ . In other parts of the phase diagram the vortices have a nonaxisymmetric double core, filled with the planar phase [28]; there is direct experimental evidence for the asymmetry of the vortex cores [29]. A third vortex type in  $^3\text{He-B}$ , the spin-mass vortex, has been discovered recently [13]. They are created when the sample is cooled through the A-B transition under rotation. Also a vortex-free Landau state, in which only the normal component rotates with the container while the superfluid component stays at rest, can be created in  $^3\text{He-B}$  [30,31].

The effect of vortices on the  $^3\text{He-B}$  texture is very different from that in  $^3\text{He-A}$ . Soft vortex cores, in which the  $\hat{\mathbf{n}}$ -vector is locally perturbed from its bulk orientation by each vortex, are present only in high magnetic fields [32]. The results of NMR-experiments [33] and of our acoustic studies [P4] (see Section 2.3.1.) support the idea that, in addition to hard cores, the  $^3\text{He-B}$  vortices also have soft cores for  $H \gtrsim 100\text{ mT}$ . However, most experiments have been performed in much lower fields, where the magnetic healing length  $\xi_H \propto 1/H$  exceeds the intervortex distance: the  $\hat{\mathbf{n}}$ -texture thus cannot follow each individual vortex. For stationary  $^3\text{He-B}$  in a long, cylindrical container, subjected to an axial magnetic field, the  $\hat{\mathbf{n}}$ -texture is of the flare-out type [34], depicted in Fig. 2b. In a rotating sample the texture remains qualitatively similar; vortices only tend to turn the  $\hat{\mathbf{n}}$ -vector away from the direction of  $\mathbf{H}$  in most parts of the sample. In rotating vortex-free  $^3\text{He-B}$ , several variations of the flare-out texture have been observed, with different boundary conditions for the angles  $\alpha$  and  $\beta$  defined in Fig. 2b [30,31,35].

### 1.3. Propagation of ultrasound in $^3\text{He}$

One of the greatest triumphs of Landau's phenomenological theory for normal Fermi liquids was the prediction, prior to observations, of the existence of a new sound mode in  $^3\text{He}$ , the zero sound [36]. Propagation of the usual hydrodynamic "first" sound is based on collisions between particles. In normal  $^3\text{He}$  the time interval  $\tau$  between quasiparticle collisions in-

creases as  $\tau \propto T^{-2}$  when temperature is decreasing: propagation of sound becomes increasingly difficult, and the attenuation  $\alpha$  grows like  $\alpha \propto \omega^2 \tau \propto \omega^2/T^2$ , where  $\omega$  is the angular frequency of sound. However, when the temperature reaches a value for which  $\omega\tau \approx 1$ , pressure waves start propagating as zero sound. That mode owes its existence to the molecular fields originating from interparticle Fermi-liquid interactions and, therefore, does not require collisions. Instead, collisions between quasiparticles attenuate the zero sound, such that  $\alpha \propto \tau^{-1} \propto T^2$ . Zero sound in normal liquid  $^3\text{He}$  was detected for the first time in 1963 [37].

Soon after the superfluid phases of  $^3\text{He}$  were discovered, Lawson *et al.* [38] demonstrated that zero sound can also propagate in  $^3\text{He-A}$ ,  $^3\text{He-B}$ , and  $^3\text{He-A}_1$ , as a collective order-parameter oscillation. However, in superfluid  $^3\text{He}$  there are new attenuation mechanisms which are not present in the normal phase [39,40,41]. Firstly, zero sound can break Cooper pairs of the superfluid condensate, provided that the sound frequency  $f$  is such that  $hf > 2\Delta$ , i.e., if the phonons have sufficient energy to remove both constituents of a Cooper pair over the gap edge  $\Delta$ . Secondly, ultrasound can excite other collective modes, which are oscillations of the superfluid order parameter about its equilibrium value:  $A_{\mu j} = A_{\mu j}^0 + \delta A_{\mu j}$ , where  $A_{\mu j}^0$  is the equilibrium order parameter, given by Eqs. (2) and (3) for  $^3\text{He-A}$  and  $^3\text{He-B}$ , respectively. For both phases, a total of 18 collective modes exist, because of the 18 independent components of the order parameter. The effect of collisions between the "normal" quasiparticles is mainly to broaden the collective mode resonances, especially near  $T_c$ ; their number density decreases exponentially for  $T \rightarrow 0$ .

### 1.3.1. Anisotropic sound propagation in $^3\text{He-A}$

In  $^3\text{He-A}$ , the propagation of zero sound is strongly anisotropic owing to the anisotropy of the energy gap  $\Delta_A(\mathbf{k}, T)$ . The attenuation  $\alpha$  and the phase velocity  $c$  of ultrasound can be written as [42]

$$\alpha = \alpha_{\parallel} \cos^4\gamma + 2\alpha_c \cos^2\gamma \sin^2\gamma + \alpha_{\perp} \sin^4\gamma \quad (11)$$

and

$$c = c_0 - \Delta c_{\parallel} \cos^4\gamma - 2\Delta c_c \cos^2\gamma \sin^2\gamma - \Delta c_{\perp} \sin^4\gamma, \quad (12)$$

respectively, where  $\gamma$  is the angle between the orbital anisotropy axis  $\hat{l}$  and the direction  $\hat{q}$  of sound propagation;  $c_0 \approx 200 \dots 400$  m/s is the velocity of zero sound in the normal phase. The components  $\alpha_i$  and  $\Delta c_i$  (for  $i = \parallel, c, \perp$ ) depend on external parameters such as temperature, pressure, ultrasonic frequency, and magnetic field.

In  $^3\text{He-A}$  the breaking of Cooper pairs by ultrasound is possible for any temperature and at any frequency since the energy gap displays nodes in the direction of  $\hat{l}$  (and  $-\hat{l}$ ). Acoustic attenuation is also modified by three collective modes: the clapping, normal flapping, and superflapping modes. The calculated temperature dependence of their resonance frequencies is presented in Fig. 3. The *clapping* (cl) *mode* corresponds to clapping-like oscillations of the  $\hat{m}$  and  $\hat{n}$  vectors of the A-phase order parameter, Eq. (2); it only affects the components  $\alpha_{\perp}$  and  $\Delta c_{\perp}$  in Eqs. (11) and (12). The *normal flapping* (nfl) *mode* can be illustrated as an oscillatory tilting of the  $\hat{l}$ -vector or, equivalently, a flapping motion of  $\hat{m}$  and  $\hat{n}$  out of their equilibrium plane. The restoring force is produced by the normal component of the fluid. This mode can

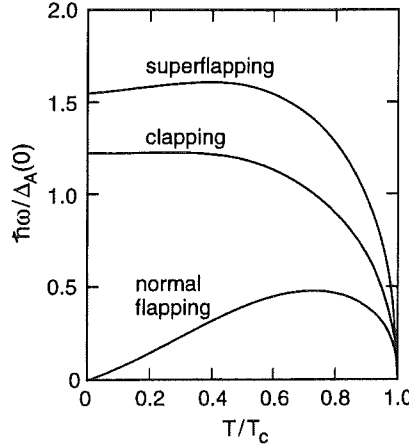


**Figure 3.** Frequencies of the collective superflapping (sfl), clapping (cl), and normal flapping (nfl) modes of  $^3\text{He-A}$  as functions of temperature, scaled by  $\Delta_A(0) = 2.03 k_B T_c$  [6].

give rise to two peaks in  $\alpha_c$  (and  $\Delta c_c$ ): one near  $T_c$  and the other, the *re-entrant nfl-mode*, in the low temperature end (see Fig. 3). The *superflapping* (sfl) mode can couple to ultrasound only at frequencies above 50 MHz. None of the collective modes contribute to the "parallel" components  $\alpha_{||}$  and  $\Delta c_{||}$ , which are determined merely by pair breaking and quasiparticle collisions.

### 1.3.2. Collective modes in $^3\text{He-B}$

The collective modes in  $^3\text{He-B}$  are eigenstates of the twisted total angular momentum  $\mathbf{J}$  with components  $J_j = L_j + R_{\mu j} S_\mu$  (summation over  $\mu$ ), where  $\mathbf{L}$  and  $\mathbf{S}$  are the orbital and spin angular momenta, respectively [43]. The 18 collective modes can be classified by the quantum numbers  $J\zeta$  and  $m_j$ . Angular momentum may obtain the values  $J = 0, 1$ , and  $2$ , its projection to a quantization axis  $m_j = -J, -J+1, \dots, J$ , and the signature  $\zeta$  is  $+$  or  $-$  for the oscillations of the real or imaginary parts of  $A_{\mu j}$ , respectively. The "imaginary" modes predominantly couple to density fluctuations, while the "real" modes interact with spin-density fluctuations. The frequencies of the modes with a common  $J$  and  $\zeta$  but with different  $m_j$  are degenerate for vanishing magnetic field ( $H = 0$ ) and wave number ( $q = 0$ ).

Zero sound propagates in  $^3\text{He-B}$  as the  $J\zeta = 0^-$  mode, whose dispersion relation is linear and  $\omega = 0$  at  $q = 0$ . The other collective modes that are important in acoustic studies are those with  $J = 2$ . The five  $2^-$  modes, called the *squashing* (sq) modes, couple to ultrasound very strongly and cause a high attenuation peak near  $T_c$ . Their resonance frequency at  $H = 0$  and  $q = 0$  is  $\omega_{sq} = \sqrt{12/5} \Delta(T)/\hbar$ , according to the weak-coupling BCS-theory without Fermi-liquid corrections. Their real counterparts, the *real squashing* (rsq,  $2^+$ ) modes with the resonance frequency  $\omega_{rsq} \approx \sqrt{8/5} \Delta(T)/\hbar$ , are excited by ultrasound as well, though weakly [44]. The coupling arises from the particle-hole asymmetry [45]: there is a small difference in the density of states above and below the Fermi surface. There are no nodes in the energy gap of

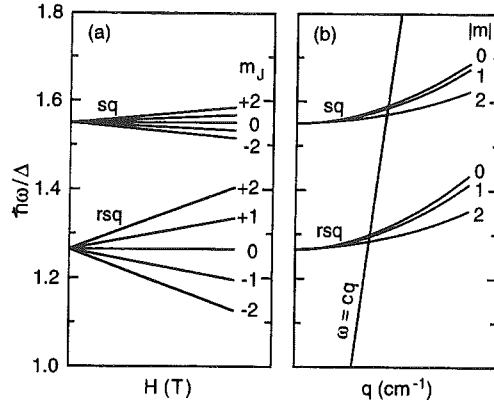


**Figure 4.** (a) Linear five-fold Zeeman splitting of the  $J = 2$  collective modes in an applied magnetic field for  $q = 0$ . (b) The dispersion curves of the  $J = 2$  modes in the absence of a magnetic field, showing the three-fold splitting for finite wave numbers. A mode can be excited in a linear process only when the dispersion lines of the mode and of zero sound cross, at  $\omega = cq$ .

$^3\text{He-B}$ , which means that there is a well-defined "pair-breaking edge": acoustic breaking of Cooper pairs is possible only for  $\omega > 2\Delta(T)/\hbar$ . An interesting peak-antipeak structure in ultrasound attenuation has been observed near this edge [46]. Such features have been interpreted as yet another collective mode, the  $J^\zeta = 1^-$  "gap mode" [47], but with some discussion about the validity of this assessment [48].

The degeneracy of the different  $m_J$ -substates having the same  $J^\zeta$  is lifted by an external magnetic field (*Zeeman effect*) [49] and also, to some extent, by the dispersion due to the non-vanishing wave vector of the mode [50]. These effects are shown schematically in Fig. 4. The Zeeman-splitting of the real squashing mode can be observed very distinctly in ultrasonic experiments [51]: five separate attenuation peaks appear, corresponding to resonances of the substates with  $m_J = 0, \pm 1$ , and  $\pm 2$ . The coupling of ultrasound to the modes with different  $m_J$  projections depends on the angle between the quantization axis  $\hat{\mathbf{h}}$  and the wave vector  $\mathbf{q}$  of the excited mode;  $\hat{\mathbf{h}}$  is defined by Eq. (5) and, in bulk liquid, points to the direction of external magnetic field, and  $\mathbf{q}$  is in the linear case determined by the wave vector of ultrasound. When  $\hat{\mathbf{h}} \parallel \mathbf{q}$ , only the submode with  $m_J = 0$  couples to sound.

The Zeeman-splitting of the rsq-mode is almost linear in  $H$ , of the form  $\omega_{\text{rsq},m_J} \approx \omega_{\text{rsq},0} + m_J g \gamma_g H$ , in magnetic fields from about 20 to 70 mT. If the dispersion correction due to finite  $q$  is taken into account, the rsq-frequencies can in this field range be written as [52]

$$\omega_{\text{rsq},m_J}^2 = \omega_{00}^2 + 2m_J \omega_{00} g \gamma_g H + c_a^2 q^2 + \frac{1}{2} c_b^2 q^2 \left[ \frac{1}{3} \left( 1 + \frac{1}{2} m_J^2 \right) + (\hat{\mathbf{q}} \cdot \hat{\mathbf{h}})^2 \left( 1 - \frac{1}{2} m_J^2 \right) \right] \quad (13)$$

where  $g \approx 0.14$  is the effective Landé g-factor,  $\gamma_g = 2.04 \cdot 10^{-8} \text{ s}^{-1} \text{ T}^{-1}$  is the gyromagnetic ratio, and  $\omega_{00} = a_{\text{rsq}} \Delta(T)/\hbar$  with  $a_{\text{rsq}} \approx \sqrt{8/5}$ . Theoretical values for the dispersion parameters are  $c_a^2 = 0.224 v_F^2$  and  $c_b^2 = 0.327 v_F^2$  (without Fermi-liquid and higher-order pairing con-

tributions) [53], where  $v_F \approx 30 \dots 60$  m/s is the Fermi velocity. Large magnetic fields ( $\gtrsim 70$  mT) deform the B-phase energy gap so much that Eq. (13) loses its validity and terms quadratic in  $H$  become important (Paschen-Back effect) [54,55].

For  $H = 0$  the dispersion relations for the rsq-submodes are [52]

$$\omega_{\text{rsq},|m|}^2 = \omega_{00}^2 + v_{|m|}^2 q^2, \quad (14)$$

where  $|m|$  assumes the values 0, 1, and 2. The modes with different  $|m|$  have different frequencies, but the three-fold dispersion splitting should not be observable in experiments involving linear acoustics because only the substate with  $|m| = 0$  couples with ultrasound for  $H = 0$  (see, however, Ref. [56] and our nonlinear experiments described in Section 2.4.2 [P8,P9]). Using the parameters of Eq. (13), the mode velocities can be expressed as

$$v_{|m|}^2 = c_a^2 + \frac{1}{6}(4 - |m|^2)c_b^2, \quad (15)$$

and we obtain  $v_0^2 = 0.442 v_F^2$ ,  $v_1^2 = 0.388 v_F^2$ , and  $v_2^2 = 0.224 v_F^2$ . The quantization axis of the modes at  $H = 0$  is  $\hat{q}$ . With increasing magnetic field the quantization axis turns smoothly from  $\hat{q}$  to  $\hat{h}$ , and the mode frequencies evolve towards those given by Eq. (13) [52,57]. It must be realized that the quantum numbers  $|m|$  at  $H = 0$  do not correspond to the quantum numbers  $m_J$  of Eq. (13), unless  $\hat{q} \parallel \hat{h}$ . For example, the  $|m| = 2$  state at  $H = 0$  does not necessarily split into the  $m_J = \pm 2$  states for  $H > 0$ .

### 1.3.3. Nonlinear acoustics

The field of nonlinear acoustics in superfluid  $^3\text{He}$  was pioneered by Polturak *et al.* [58]. They studied the transmission of ultrasound pulses through  $^3\text{He}$ -B with acoustic energy densities up to about  $10 \text{ nJ/cm}^3$ , which is about 1% of the superfluid condensation energy density  $U_c$  under their experimental conditions;

$$U_c = \frac{1}{2} N(E_F) \Delta^2(T), \quad (16)$$

where  $N(E_F)$  is the single spin density of states at the Fermi surface. Polturak *et al.* observed saturation of zero-sound attenuation and break-up of the sound pulses near the rsq-resonance. Their results have been interpreted in terms of soliton propagation and self-induced transparency [58,59], based on similar effects in nonlinear optics. However, there are both qualitative and quantitative discrepancies between the experimental data and the soliton model [60,61].

Nonlinear acoustic phenomena have been observed in the A-phase as well [62]. At low temperatures the sample became almost transparent to ultrasound at high acoustic intensities. Energy densities two to three orders of magnitude below  $U_c$  were enough to develop the transparency fully. These results could well be explained by an "evoked two-level system" model. We have performed further investigations on this phenomenon [P1]. They are discussed in Section 2.2.1.

Quite different types of nonlinear phenomena are parametric processes, which involve the absorption and emission of modes with different frequencies [63]. Such processes have

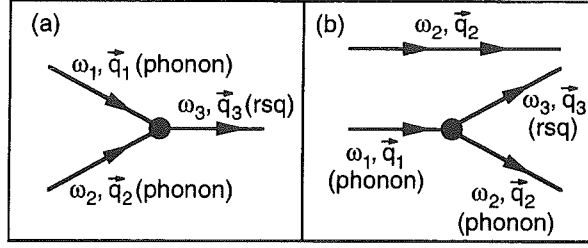


**Figure 5.** Schematic presentations of (a) two-phonon absorption and (b) stimulated Raman scattering by the rsq-mode in  $^3\text{He-B}$ .

been extensively studied in nonlinear optics [64]. These concepts were first applied to the case of acoustics in superfluid  $^3\text{He}$  by Serene [65], who predicted the generation of sound with third harmonic frequency of excitation in  $^3\text{He-B}$ . So far this phenomenon has not been observed experimentally. McKenzie and Sauls [63,66,67] have performed an extensive theoretical study on parametric processes in  $^3\text{He-B}$ . Especially, they predicted the two-phonon absorption (TPA) and the stimulated Raman scattering by the rsq-mode. Our observation of TPA is the first experimental verification of nonlinear parametric acoustic processes in superfluid  $^3\text{He}$  [P7 – P9].

Two-phonon absorption is conceptually a very simple process: phonons, with angular frequencies  $\omega_1$  and  $\omega_2$  and wave vectors  $\mathbf{q}_1$  and  $\mathbf{q}_2$ , excite together a quantum of collective mode with  $\omega_3$ ,  $\mathbf{q}_3$ , so that the energy and momentum are conserved, i.e.,  $\omega_1 + \omega_2 = \omega_3$  and  $\mathbf{q}_1 + \mathbf{q}_2 = \mathbf{q}_3$  (see Fig. 5a). The inverse process, in which a phonon with frequency  $\omega_1$  decays into a phonon with a lower frequency  $\omega_2$  and a collective-mode quantum with  $\omega_3 = \omega_1 - \omega_2$ , in the presence of a sound wave with frequency  $\omega_2$ , is called stimulated Raman scattering and is shown schematically in Fig. 5b.

Coupling of the collective modes to ultrasound in the linear or nonlinear processes depends on the selection rules arising from the approximate particle-hole symmetry of  $^3\text{He}$ . As was discussed in Section 1.3.2, zero sound couples strongly with the squashing mode in linear processes, whereas there is only a weak coupling between zero sound and the real squashing mode, arising from the weak violation of the particle-hole symmetry. The situation is reversed in the case of the two-phonon processes: the rsq-mode can be excited by ultrasound but the sq-mode cannot, except again for the very weak contribution due to particle-hole asymmetry.

Two-phonon processes can be experimentally observed by simultaneously sending two overlapping sound waves with different frequencies through the sample. When the sum or difference of the two acoustic frequencies is in resonance with the rsq-mode, there should be an anomaly in attenuation. If the signal wave, which is monitored, is of much lower intensity than the pump wave, the size of the anomalies in attenuation  $\alpha$  and phase velocity  $c$  of the signal wave should be [66]

$$\frac{\Delta\alpha}{\alpha_s} \simeq \frac{\Delta c}{c} \simeq \frac{|\tilde{A}|^2}{(1 + F_0^s)^2} \frac{\Delta(T)}{\Gamma} \frac{U_p}{U_c} . \quad (17)$$

Here  $q_s$  is the wave number of the signal wave,  $\tilde{A}$  is the coupling strength which has been calculated with the microscopic theory [63],  $F_0^s$  is a Landau Fermi-liquid parameter,  $1/\Gamma$  is the lifetime of the mode,  $U_p$  is the energy density of the pump wave, and  $U_c$  is the superfluid condensation energy density given by Eq. (16). Nonlinear features should thus be strongest at low pressures where  $F_0^s$  is small, and for low temperatures where  $1/\Gamma$  is large.

## 2. Acoustic experiments

### 2.1. Experimental techniques

Experiments reported in this thesis were performed in the rotating nuclear demagnetization cryostat ROTA2, which has been described in detail elsewhere [68,69,70]. Cryogenic techniques in general have been discussed in Refs. [71] and [72]. The experimental region of the apparatus, from the bottom of the dilution refrigerator to the top of the copper nuclear stage, is illustrated in Fig. 6. The Pt-NMR thermometer probe, the heat exchanger between the  $^3\text{He}$ -sample and the nuclear stage, the experimental magnet, and the ultrasonic cell are shown.

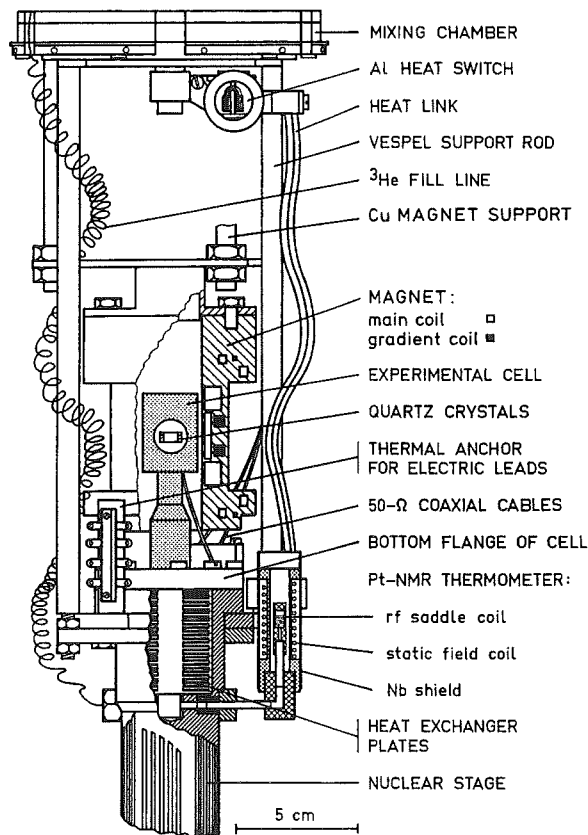


Figure 6. Inner parts of the ROTA2-cryostat [68,69,70].



The Pt-NMR thermometer probe is located in a separate tower. Its platinum powder is immersed in  $^3\text{He}$  which is in liquid contact to helium in the bottom part of the heat exchanger through a 70 mm long Cu-Ni tube of 3-mm inner diameter. The heat exchanger was made of 14 silver disks, each of which had silver sinter on both surfaces. After sintering the disks were electron-beam welded together, and the stack likewise welded from the top into a large-bore pit on the upper end of the copper nuclear stage. The nominal surface area of the sinter is about  $100\text{ m}^2$ , and measurements of thermal relaxation between  $^3\text{He}$  and the nuclear stage yielded an effective area of about  $30\text{ m}^2$ . Good performance of the heat exchanger was crucial for the success of our nonlinear experiments, in which very energetic sound pulses had to be applied to the sample.

The experimental magnet, hanging from the bottom of the mixing chamber of the dilution refrigerator, consists of two parts: the main solenoid which can generate an axial field of more than 1 T with an inhomogeneity of less than  $10^{-3}$  inside the experimental volume, and a gradient magnet which can produce a linear axial field gradient up to about 15 mT/mm. The magnets were wound of 0.17 mm multifilamentary Nb-Ti wire with a copper matrix (main magnet) or a CuNi matrix (gradient magnet) on a reinforced glass-fiber epoxy former. With superconducting joints made using pressed Nb-Ti ferrules, a 10 A current could be persisted in both magnets. The stray fields of the magnets were carefully minimized to prevent thermal load caused by magnetized copper: Even though the center of the experimental chamber was only 50 mm above the bottom flange of the cell, and the diameter of the inner bore of the magnet was as large as 26 mm, the maximum field on the copper parts below the magnet was only about 0.5% of the field applied to the ultrasonic chamber. The high field of the main magnet made possible the first experiments on rotating  $^3\text{He-A}_1$  [73], and the gradient magnet enabled us to keep the A-B phase boundary between the sound crystals continuously for tens of minutes.

Two different ultrasound chambers were used, both of them encapsulated into an epoxy container (see Fig. 6). Most of the experiments were performed in the cylindrical cell shown in Fig. 7a. It consists of two X-cut quartz crystals with their fundamental frequency at 8.9 MHz, separated by a 4 mm thick annular quartz spacer with a 6-mm inner diameter. Ultrasound propagated parallel to the rotation axis of the cryostat and the external magnetic field. A new cubic cell (Fig. 7b) was used in some of our nonlinear experiments. It has four quartz crystals each with the basic frequency 5 MHz, mounted on two vertical and two horizontal faces of a  $9.5 \times 9.5 \times 9.5\text{ mm}^3$  cube made of Macor glass. The sample space is formed by three crossed holes of diameter 6 mm, bored through each side of the solid cube as shown in Fig. 7b.

In all experiments we used the pulsed transmission technique: one crystal was employed for sending the ultrasound, and the other received the sound pulse after it had travelled through the sample. The length of the drive pulses was typically 12  $\mu\text{s}$  in the cylindrical cell and 45  $\mu\text{s}$  in the cubic chamber; the lengths were chosen so that the sound pulse that had propagated directly from the transmitter to the receiver was clearly separated from echoes. The envelopes of the sound pulses were not rectangular, like the electrical drive, but they were rounded because of the resonant nature of the quartz crystals; their ringing time is about



by  $A(x) = A_n \exp(-\alpha x)$ , where  $A_n$  is the sound amplitude transmitted and  $A(x)$  its value at a distance  $x$  from the transmitter, was determined with respect to the value just above  $T = T_c$ :

$$\alpha(T) - \alpha(T_c) = -\frac{1}{L} \ln[A(T)/A(T_c)] , \quad (19)$$

where  $L$  is the distance between the transmitter and the receiver crystals. The phase velocity  $c = \omega q$  of ultrasound can be calculated from the phase of the received signal,  $\varphi = \arctan\left(\int_{t_1}^{t_2} a_{\text{out}} dt / \int_{t_1}^{t_2} a_{\text{in}} dt\right)$ , as follows:

$$\frac{c(T) - c(T_c)}{c(T_c)} = -\frac{\varphi(T) - \varphi(T_c)}{\omega L / c(T_c) + \varphi(T) - \varphi(T_c)} , \quad (20)$$

where  $\omega = 2\pi f$  is the angular frequency of the ultrasound.

In our nonlinear experiments two sound pulses with different frequencies were sent simultaneously through the sample. This was done either by exciting the transmitter crystal concurrently with two frequencies or, in the cubic cell, sending the two waves from two different, mutually perpendicular crystals. This is discussed in more detail in Publication [P9].

## 2.2. Investigations of $^3\text{He-A}$

One of the original motivations for starting the acoustic experiments in the ROTA2-cryostat was to gain new information on vortices in  $^3\text{He-A}$ . The main advantage of ultrasound compared to NMR as a probe of vortices is that measurements can be performed at any magnetic field, from  $H = 0$  to  $H > 1$  T. Our experiments at low fields revealed a new vortex type [P1], and rotating  $^3\text{He-A}_1$  (see the phase diagram in Fig. 1) was studied in high fields for the first time [73]. However, differences between the expected ultrasonic responses of different vortex types in  $^3\text{He-A}$  are so small and the quantitative analysis of the acoustic data is so complicated that very accurate conclusions about the vortex structures cannot be made yet [P4]. Before discussing vortices in more detail, our experiments on stationary  $^3\text{He-A}$  at low temperatures will be described.

### 2.2.1. Re-entrant normal flapping mode

An anomalous increase of ultrasonic attenuation in  $^3\text{He-A}$  at low pressures and low temperatures was first detected by Piché *et al.* [75]. The authors interpreted their data in terms of pair breaking and suggested that the results imply a strong deviation of the A-phase energy gap from its BCS-value at low temperatures and pressures. However, our experiments [P1] show that the anomalous behavior is caused by the re-entrant normal flapping mode, which can couple to ultrasound at low temperatures (see Fig. 3).

We performed our experiments in a similar geometry as Piché *et al.* [75]: the sample cell (Fig. 7a) had the same dimensions, and the A-phase was stabilized at low temperatures (see the phase diagram in Fig. 1) by a magnetic field  $H \approx 0.3 \dots 1$  T, applied parallel to the direction of ultrasound propagation  $\hat{q}$ . The field holds  $\hat{d} \perp \hat{q}$ , and in the bulk liquid the orbital anisotropy axis  $\hat{l}$  is perpendicular to  $\hat{q}$  as well, because of dipolar interaction. Thus the acoustic attenuation is given by the component  $\alpha_{\perp}$  in Eq. (11). However,  $\hat{l}$  turns away from its

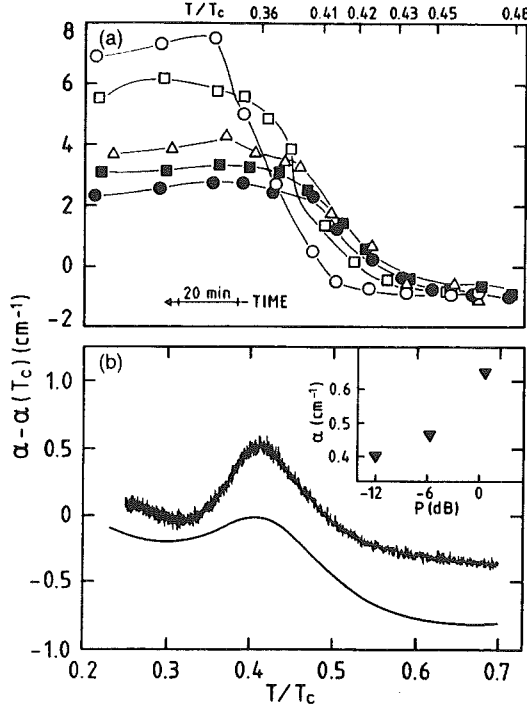


**Figure 8.** Attenuation of zero sound in  $^3\text{He-A}$  at (a)  $p = 0$ ,  $f = 8.9$  MHz, and  $H = 350$  mT, and at (b)  $p = 9.3$  bar,  $f = 26.8$  MHz, and  $H = 1.025$  T [P1,70]. In both cases  $\mathbf{q} \parallel \mathbf{H}$ . The energy of the largest pulses in (a) (open circles) was about 5 pJ. In the other traces, the pulses were decreased by 10 dB (open squares), 20 dB (open triangles), 30 dB (filled squares), and 40 dB (filled circles), respectively. In (b), the upper trace is one experimental recording, measured with "0 dB" sound pulses, and the lower solid line is the calculated attenuation, taking into account the texture in our experimental cell [77]. The inset shows the peak height as a function of the excitation level.

bulk orientation within the dipolar length  $\xi_d$  from the ultrasonic crystals, because  $\hat{l}$  must be normal to solid walls. Inside this surface layer, the attenuation is affected also by  $\alpha_{\parallel}$  and, more importantly for the present discussion, by  $\alpha_c$ . This effect was underestimated in Ref. [75]. Because  $\xi_d$  increases from 10  $\mu\text{m}$  at  $p = 30$  bar to 50  $\mu\text{m}$  at zero pressure, the importance of the boundary layer increases towards lower pressures.

Our results at zero pressure, with  $f = 8.9$  MHz, are shown in Fig. 8a. Acoustic attenuation increases with decreasing temperature below  $T \approx 0.45T_c$ , and a maximum is reached for  $T \lesssim 0.35T_c$ . Attenuation  $\alpha_{\perp}$  in the bulk liquid is supposed to be almost constant and very small in this temperature interval; it is only determined by pair breaking and above  $0.9T_c$  by the clapping mode (see Section 1.3.1). The attenuation maximum is caused by the re-entrant normal flapping mode [76], which produces a peak in  $\alpha_c$  for  $T/T_c \approx 0.29$  under the conditions of Fig. 8a. This temperature is very close to the position of the observed attenuation maximum. The mode couples to ultrasound in the dipolar boundary layer, where  $\gamma \neq 0$  and  $\gamma \neq \pi/2$  (see

Eq. (11)). Piché *et al.* [75] could not detect the attenuation maximum because the expected temperature for the re-entrant nfl-mode for their experimental conditions ( $f = 14.8$  MHz,  $p = 0$ ) is  $T/T_c \approx 0.49$  (see Fig. 3), which is just below their minimum temperature. Fig. 8b shows our results for  $f = 26.8$  MHz and  $p = 9.3$  bar, together with a theoretical prediction [77] for attenuation produced by the dipolar surface layer in our chamber. The peak corresponding to the re-entrant nfl-mode is very clear and consistent with theory.

Fig. 8a shows that propagation of sound pulses in the vicinity of the nfl-mode is nonlinear: attenuation depends on the amplitude of sound. The five traces in Fig. 8a were obtained using acoustic powers differing by four orders of magnitude. The maximum energy (0 dB) of the 12- $\mu$ s pulses used in these measurements was less than 5 pJ, i.e., about two orders of magnitude smaller than the energies of the pump pulses in our nonlinear experiments on  $^3\text{He-B}$  [P7 – P9] (see Section 2.4).

On the "wing" of the nfl-mode at  $0.40 \lesssim T/T_c \lesssim 0.45$  the attenuation of the sound pulses decreases with increasing amplitude. Such behavior was first observed by Avenel *et al.* [62], using the same experimental setup as in Ref. [75]. A semi-phenomenological two-level model could explain their data very well. The model was based on the assumption that the anomalous attenuation is caused by pair breaking, but the situation near the wings of the collective modes in  $^3\text{He-A}$  should be very similar [78].

Quite surprisingly, Fig. 8a and the inset of 8b show that just at the attenuation peak the nonlinearity is reversed: strong pulses are attenuated more than weak ones. The peak heights measured by the smallest sound pulses are in agreement with our model of coupling to the nfl-mode on the dipolar boundary layer. We repeated the experiment at  $p = 0$  also by keeping the amplitude of excitation constant but, instead, changing the length of the sound pulses between 1 and 12  $\mu$ s. Again the short pulses were attenuated more than the long ones at the wing of the mode, whereas at the peak the situation was reversed. One should note that we determined the attenuation  $\alpha$  from the areas under the pulse components received, according to Eqs. (18) and (19). It may be that such an analysis is not suitable near the peak where the received pulse becomes distorted [P1], so that the observed reversal in nonlinearity may be an experimental artefact.

### 2.2.2. Rotating $^3\text{He-A}$ in low magnetic fields: vortex transition

Continuous vortices of  $^3\text{He-A}$  have a different structure in low magnetic fields ( $H \ll H_d$ ) than in high fields ( $H \gg H_d$ ) [8]. When  $H \gg H_d \approx 3$  mT, the magnetic healing length  $\xi_H \propto 1/H$  is smaller than the dipolar length  $\xi_d \approx 10$   $\mu$ m, as was discussed in Section 1.1: the  $\hat{\mathbf{d}}$ -texture is affected more by the magnetic field than by the  $\hat{\mathbf{l}}$ -texture. The field forces  $\hat{\mathbf{d}} \perp \mathbf{H}$  everywhere, and the  $\hat{\mathbf{l}}$ -vector deviates from the direction of  $\hat{\mathbf{d}}$  inside the so-called *dipole-unlocked* soft core, whose size is determined by  $\xi_d$  (see Figs. 2a and 9a). On the other hand, when  $H < H_d$  and  $\xi_H > \xi_d$ , the  $\hat{\mathbf{d}}$ -vector is locked to the direction of  $\hat{\mathbf{l}}$  by dipolar forces also within the vortex cores (see Fig. 9b). Then the two vectors deviate from the plane perpendicular to  $\mathbf{H}$  inside the *dipole-locked* core, whose size is determined by  $\xi_H$  which increases with decreasing  $H$ . What is interesting is that these two structures cannot change continuously to each other, because they are topologically different. There must be a first order transition

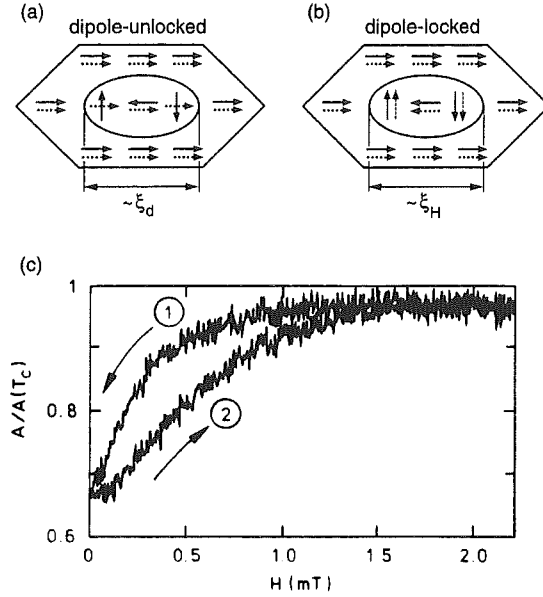


**Figure 9.** Schematic illustration of the  $\hat{l}$  (solid arrows) and  $\hat{d}$  (dashed arrows) textures of (a) the dipole-unlocked Seppälä-Volovik vortex [25] and (b) the dipole-locked Anderson-Toulouse vortex [82]. (c) The sound amplitude received during a sweep of the magnetic field at  $p = 26.7$  bar,  $\Omega = 0.3$  rad/s,  $T/T_c \approx 0.9$ , and  $f = 26.8$  MHz. In trace 1 (2) rotation was started at  $H = 2.2$  mT ( $H = 0$ ) and the field was swept down (up) [P2,79].

between the dipole-locked and the dipole-unlocked vortices, which was detected in our experiments [P2,80].

The important topological invariant for the present discussion is the winding number  $\tilde{m}_d$ , which shows how many times the tip of the  $\hat{d}$ -vector covers the unit sphere inside the vortex core. The winding number can be defined as

$$\tilde{m}_d = \frac{1}{4\pi} \int_{\sigma} \sin \theta(x, y) \frac{\partial(\theta, \varphi)}{\partial(x, y)} dx dy, \quad (21)$$

when  $\hat{d}(x, y)$  is presented in spherical coordinates, using the polar angle  $\theta$  and the azimuthal angle  $\varphi$ ;  $x$  and  $y$  are spatial coordinates in a plane perpendicular to the axis of the vortex. The integration area  $\sigma$  is chosen so that it contains one soft vortex core or, if the lattice consists of different types of vortices, one elementary Wigner-Seitz cell of the lattice. The Jacobian is given by

$$\frac{\partial(\theta, \varphi)}{\partial(x, y)} = \begin{vmatrix} \partial\theta/\partial x & \partial\theta/\partial y \\ \partial\varphi/\partial x & \partial\varphi/\partial y \end{vmatrix}. \quad (22)$$

Note that the integral in Eq. (21) is nothing but the area of a unit sphere,  $\int \sin \theta d\theta d\varphi$ , expressed using the variables  $x$  and  $y$  which are not necessarily in one-to-one correspondence with  $\theta$  and  $\varphi$ .

Expression (21) can be written in another form [8], viz.,

$$\tilde{m}_d = \frac{1}{4\pi} \int_{\sigma} \hat{\mathbf{d}} \cdot (\partial_x \hat{\mathbf{d}} \times \partial_y \hat{\mathbf{d}}) dx dy \quad . \quad (23)$$

The corresponding winding number for the  $\hat{\mathbf{l}}$ -vector field is

$$\tilde{m}_l = \frac{1}{4\pi} \int_{\sigma} \hat{\mathbf{l}} \cdot (\partial_x \hat{\mathbf{l}} \times \partial_y \hat{\mathbf{l}}) dx dy \quad . \quad (24)$$

In a continuous texture, both  $\tilde{m}_d$  and  $\tilde{m}_l$  must be integers. From the Mermin-Ho relation, Eq. (10), it follows that  $\tilde{m}_l$  is connected with the number  $N$  of circulation quanta per vortex, or per elementary cell, as  $\tilde{m}_l = N/2$ .  $N$  is defined so that outside the core, where  $\nabla \times \mathbf{v}_s = 0$ , the velocity field is given by Eq. (9). Thus, for continuous vortices  $\tilde{m}_l \geq 1$  and  $N$  is even. In a dipole-locked low-field vortex, in which  $\hat{\mathbf{d}}$  follows  $\hat{\mathbf{l}}$  (Fig. 9b),  $\tilde{m}_d = \tilde{m}_l \geq 1$ . On the other hand, in the high-field vortex  $\hat{\mathbf{d}}$  stays in a plane and  $\tilde{m}_d = 0$  (Fig. 9a), even though  $\tilde{m}_l$  still has a nonzero integer value. Thus, at the critical field  $H \simeq H_d$ , a transition is expected to occur in which  $\tilde{m}_d$  jumps discontinuously from  $\tilde{m}_l \geq 1$  to zero. However, because the transition is of first order, metastability effects are important.

Figure 9c shows two traces of the received ultrasound amplitude  $A$ , scaled by the value at  $T_c$ , versus the external magnetic field. The cryostat was rotated at  $\Omega = 0.3$  rad/s at  $p = 26.7$  bar and  $T/T_c \simeq 0.9$ .  $A/A(T_c)$  is related to the effective attenuation  $\alpha$  according to Eq. (19) (see, however, Section 2.2.3). The upper curve (1) was measured by starting rotation at  $H = 2.2$  mT, which is strong enough for the creation of high-field vortices, and sweeping the field down to zero within 8 minutes while rotating the cryostat. During the sweep the vortices were of the high-field type with a dipole-unlocked soft core (see Fig. 9a), which remains metastable down to  $H = 0$ . The rotation response of the dipole-locked low-field vortices (trace 2) was obtained by starting rotation at  $H = 0$  and then sweeping the field up. The two curves are clearly dissimilar.

The topological transition takes place in the  $\hat{\mathbf{d}}$ -vector field, but ultrasound is sensitive to the distribution of the  $\hat{\mathbf{l}}$ -vector: the sizes of the regions where the components  $\alpha_{\parallel}$ ,  $\alpha_c$ , and  $\alpha_{\perp}$  (Eq. (11)) are important, are different for the different  $\hat{\mathbf{l}}$ -textures. However, the  $\hat{\mathbf{l}}$ -vector distribution in the low-field vortices is also different from that in the high-field vortices. Even if the  $\hat{\mathbf{l}}$ -field had a similar structure for both vortex types, as in Fig. 9, there would be a difference in the size of the soft vortex core, where  $\hat{\mathbf{l}}$  deviates from a plane, between the dipole-locked ( $\xi_H$ ) and dipole-unlocked ( $\xi_d$ ) vortices. Moreover, it has been suggested by Torizuka *et al.* [80] that the  $\hat{\mathbf{l}}$ -texture changes in the transition as well, from the doubly quantized Seppälä-Volovik structure [25] at high fields to the so-called Type-I structure [22,81] with  $N = 4$  at low fields. The type of the low-field vortices cannot be determined from our data.

The low-field vortices become unstable against high-field vortices at a "catastrophe field"  $H_{c1}$ . The transition cannot be seen directly in such traces as 2 in Fig. 9c because the ultrasonic response of the two vortex types is very similar above 1.5 mT. The catastrophe field was detected using the following scheme: The low-field vortices were first created by starting rotation at  $H = 0$ . The field was then swept up to  $H_{\max}$  and after that down to  $H_{\text{ref}} \simeq 0.5$  mT, at which field the two vortex types can be distinguished owing to their distinct ultrasonic responses (see Fig. 9c). When  $H_{\max}$  was below about 4 mT the vortices were still of the low-

field type (curve 2 in Fig. 9c) after the field sweeps, but when  $H_{\max}$  exceeded 4 mT they had changed to high-field vortices and their ultrasonic response followed curve 1 in Fig. 9c. The catastrophe field was  $H_{c1} \simeq 4$  mT, independent of rotation velocity.

The critical field  $H_c$  for which the two vortex types have the same free energy was determined in the following way: rotation was started at  $H = H_i$ , and then the field was swept to  $H_{\text{ref}} \simeq 0.5$  mT, where  $A/A(T_c)$  was measured. The critical field was found to be  $H_c \simeq 1.5$  mT, again independent of  $\Omega$ . When  $H_i$  was above 1.5 mT, a clear high-field vortex response at  $H = H_{\text{ref}}$  was obtained. However, the transition was not very sharp. Even for  $H_i < 1.5$  mT several of the vortices created seemed to be of the high-field type. This would suggest that at low fields Anderson-Toulouse vortices [82] are created; unlike Type-I vortices, they have similar asymptotic orientations of the  $\hat{\mathbf{l}}$ - and  $\hat{\mathbf{d}}$ -vectors outside the core as the Seppälä-Volovik vortices (see Figs. 9a and 9b) and can easily form a continuous structure together.

### 2.2.3. Rotating $^3\text{He-A}$ in high magnetic fields

In high magnetic fields (100 ... 350 mT) the vortices of  $^3\text{He-A}$  were investigated mainly by start-stop experiments: ultrasound amplitude received during rotation was compared to that measured when the cryostat was at rest [P4]. We had  $\mathbf{H} \parallel \Omega \parallel \mathbf{q}$ , so that in the stationary state the  $\hat{\mathbf{l}}$ -vector was in the plane perpendicular to the sound wave vector  $\mathbf{q}$ : acoustic attenuation was given by the component  $\alpha_{\perp}$  of Eq. (11). Inside the soft vortex cores  $\hat{\mathbf{l}}$  turns away from the plane, and also the components  $\alpha_{\parallel}$  and  $\alpha_c$  contribute to ultrasound propagation. The detected amplitude  $A$  was normally decreased by rotation because  $\alpha_c > \alpha_{\perp}$ , except very near  $T_c$ .

Experimental data on the rotation-induced change in the received sound amplitude,  $\Delta A/A_{\perp} \equiv [A(\Omega) - A(0)]/A(0)$ , versus  $\Omega$  at several conditions are shown in Fig. 10. The results are presented in terms of  $A$  instead of  $\alpha$  because we do not measure the average attenuation  $\langle \alpha \rangle$  of the vortex structure. The effective attenuation, defined by Eq. (19), is different from  $\langle \alpha \rangle$  when the attenuation profile in the sample is strongly inhomogeneous. From Fig. 10 we note that the effect of rotation is strong and nonlinear in  $\Omega$ . Under the conditions of Fig. 10b the sound signal is totally absorbed by the sample already for  $\Omega \gtrsim 2$  rad/s. If the inhomogeneity in the sound velocity is not taken into account,  $\Delta A/A_{\perp}$  should be a linear function of  $\Omega$  up to velocities where the vortex cores start to overlap. This should only take place for  $\Omega \gtrsim 25$  rad/s at high pressures.

In addition to attenuation, the velocity of sound inside the vortex cores is also different from its value in the bulk liquid (see Eq. (12)). This has two consequences which make a quantitative analysis of our data very complicated. Firstly, the sound rays traversing over different parts of the sample with an inhomogeneous velocity profile have different phases on arriving at the receiver crystal, which serves to cancel partially the signal. Secondly, sound is guided towards the velocity minima. The first theoretical considerations of these effects, starting directly from the wave equation, have already been published [83]. The data in Publication [P4] were analyzed using simple ray acoustics. However, the reliability of such an analysis is somewhat questionable since the radius of the vortex core is not much larger than the wavelength of sound.



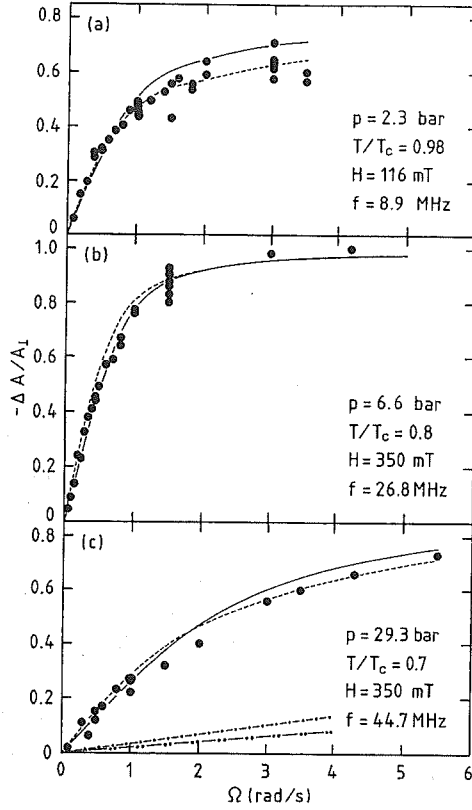


**Figure 10.** The relative change,  $\Delta A/A_{\perp}$ , of the received sound amplitude as a function of  $\Omega$  in  $^3\text{He-A}$  under three different experimental conditions [P4,70]. The solid and dashed curves represent the best fits to the measured data, calculated using ray acoustics, for continuous and singular Seppälä-Volovik vortices, respectively. In (a) the core radius is  $r_c = 50 \mu\text{m}$ , in (b)  $r_c = 45 \mu\text{m}$ , and in (c)  $r_c = 30 \mu\text{m}$  for both vortex types. The dash-dotted and dash-dot-dotted lines in (c) illustrate theoretical predictions for the continuous and singular Seppälä-Volovik vortices, respectively, assuming  $\xi_d = 10 \mu\text{m}$ .

The curves in Fig. 10 show the calculated rotation responses for singly quantized singular and doubly quantized continuous Seppälä-Volovik vortices [25]. The radius  $r_c$  of the vortex core has been chosen in each case to give the best fit to the data. The calculated response of both vortex types is, somewhat surprisingly, very similar with the same value for  $r_c$ , even though the density of vortices differs by a factor of 2 between the two textures. At  $p = 29.3$  bar, the fitted value for  $r_c$  is two (three) times larger than the theoretical value for continuous (singular) Seppälä-Volovik vortices. At low pressures the agreement is somewhat better. The discrepancy may partly be caused by the invalidity of ray acoustics for our conditions, and partly because experimental values for the coefficients  $\alpha_i$  and  $\Delta c_i$  in Eqs. (11) and (12) are not available; theoretical values calculated by Wojtanowski [77] were used, instead. In all conditions, except for  $p = 2.3$  bar and  $T/T_c = 0.95$ , the fitted  $r_c$  is in better agreement with the core

radius of continuous than singular vortices. No indication supporting the existence of more than one vortex type in our chamber at high magnetic fields was observed. A transition between singly quantized singular and doubly quantized continuous vortices should have been detected easily because the core radius in the former case is smaller by a factor of  $1/\sqrt{2}$  than that in the latter.

Our other experiments on vortices in the A-phase are discussed in Publication [P4]. They include studies of the formation and decay of vortices, and an observation of a slow relaxation process in the vortex lattice of  $^3\text{He-A}$ .

## 2.3. Linear acoustics in $^3\text{He-B}$

### 2.3.1. Rotation response in high magnetic fields

In an applied magnetic field, the energy gap of  $^3\text{He-B}$  is anisotropic and has the form given by Eq. (4). The gap has a minimum in the direction of  $\hat{\mathbf{h}}$  defined by Eq. (5). The distortion is observable in fields above about 50 mT: Ultrasound attenuation is anisotropic even outside the collective-mode peaks and can be expressed by Eq. (11); now  $\gamma$  is the angle between  $\hat{\mathbf{q}}$  and  $\hat{\mathbf{h}}$ . In the absence of other perturbations,  $\hat{\mathbf{h}}$  is along the magnetic field. Note that in  $^3\text{He-A}$  the anisotropy axis  $\hat{\mathbf{l}}$  is forced into the plane perpendicular to  $\mathbf{H}$ , instead. Rotation turns  $\hat{\mathbf{h}}$  away from the direction of  $\mathbf{H}$ , owing to interaction with vortex cores and/or counterflow  $\mathbf{w} = \mathbf{v}_s - \mathbf{v}_n$  between the normal and superfluid components.

Figure 11 shows a typical attenuation trace in a start-stop experiment in field-distorted  $^3\text{He-B}$  [P4]. Again  $\mathbf{H} \parallel \Omega \parallel \mathbf{q}$ , so that in the stationary state  $\gamma = 0$  and the attenuation component  $\alpha_{\parallel}$  is measured. The sharp minimum during acceleration is caused by counterflow which has a strong effect on the direction of  $\hat{\mathbf{h}}$  before the vortices have been created. When the vortex lattice forms and the average counterflow decreases,  $\alpha$  relaxes towards an equilibrium level. After stopping rotation, the vortices immediately decay and the attenuation returns back to  $\alpha_{\parallel}$ .

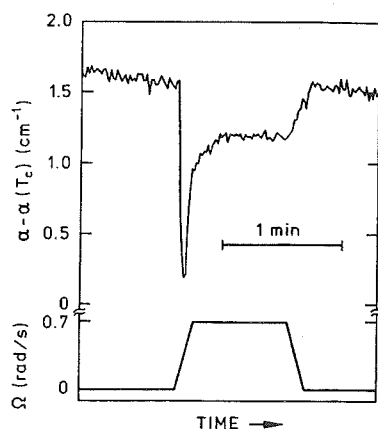


**Figure 11.** Attenuation trace in  $^3\text{He-B}$  during a start-stop experiment at  $p = 2.3$  bar,  $T/T_c = 0.86$ ,  $H = 174$  mT, and  $f = 8.9$  MHz [P4,70]. The angular velocity of the cryostat is indicated in the lower part of the figure.

The equilibrium shift  $\Delta\alpha$  of the attenuation level measured under rotation from that measured in the stationary state is a strongly nonlinear and often a nonmonotonic function of  $\Omega$ . In some cases  $\Delta\alpha$  even changes sign when  $\Omega$  is increased. A quantitative interpretation of our data is not possible, because neither theoretical nor experimental results are available about the attenuation components  $\alpha_{\perp}$  and  $\alpha_c$  in the field-distorted B-phase. However, all our results above  $H \approx 100$  mT support the existence of soft vortex cores [32], in which the  $\hat{n}$ -texture is locally distorted by each vortex, instead of the smooth flare-out texture (Fig. 2b).

The critical velocity  $\Omega_v$  for the nucleation of vortices is about 0.2 rad/s in our chamber at high fields. Above this angular velocity vortices are created with a time constant  $\tau$  which decreases with increasing  $\Omega$ . At  $\Omega = 0.4$  rad/s,  $\tau$  is between 5 and 30 s, depending on temperature, and at  $\Omega = 1$  rad/s the time constant is a few seconds. When the cryostat was accelerated slowly in the vortex-free state below  $\Omega_v$ , a kink in the attenuation showed up at  $\Omega \approx 0.1$  rad/s. This was probably caused by one of the textural transitions observed earlier in the NMR-experiments [31].

An interesting metastable state in rotating  $^3\text{He-B}$  was discovered when the sample was cooled from the A-phase into the B-phase under continuous rotation [P4,84]. The attenuation level in this state was clearly different from and had more scatter than that in the equilibrium state produced by starting the rotation in the B-phase. The attenuation in the metastable state relaxed towards the value in the equilibrium vortex state within about 10 minutes. Soon after our discovery, an anomalous flow state was detected also in NMR-experiments when the sample was in a similar way rotated through the  $A \rightarrow B$  transition [13]. That observation was interpreted in terms of spin-mass vortices (SMV). Just after the AB transition there were so many SMVs in the sample that distinctive features could be seen even in the conventional NMR signal. However, most of the SMVs decayed within about 20 minutes, and the remaining ones could be detected only when the homogeneously precessing resonance mode, HPD, was utilized [13]. It is very probable that the metastable state which we discovered was a manifestation of spin-mass vortices as well. Note that we made the experiments at  $p < 2.5$  bar,  $H \approx 100 \dots 200$  mT, whereas those of Ref. [13] were performed at  $p = 29.3$  bar,  $H = 28.4$  or 14.2 mT.

We also performed some start-stop experiments when the AB phase boundary was swept slowly (within tens of minutes) through the sample, by applying a gradient of magnetic field. The results were not very interesting, though: the B-phase response changed smoothly to that of the A-phase when the volume of  $^3\text{He-A}$  in the cell increased. Theoretically it has been predicted that very intriguing objects, such as monopoles, could exist on the AB boundary [85].

### 2.3.2. Anomalous magnetic field dependence of ultrasound attenuation

At low pressures ( $\leq 6.6$  bar), ultrasonic attenuation in  $^3\text{He-B}$  has an anomalous dependence on the external magnetic field at  $H \approx 200$  mT [P3,P4]. This is shown in Fig. 12, where the attenuation level just below the AB-transition temperature  $T_{AB}$  is presented as a function of  $H$  at several pressures. Note that the temperature changes along the  $H$ -axis, owing to the field dependence of  $T_{AB}$  (see the phase diagram in Fig. 1). Sound propagates along the direc-

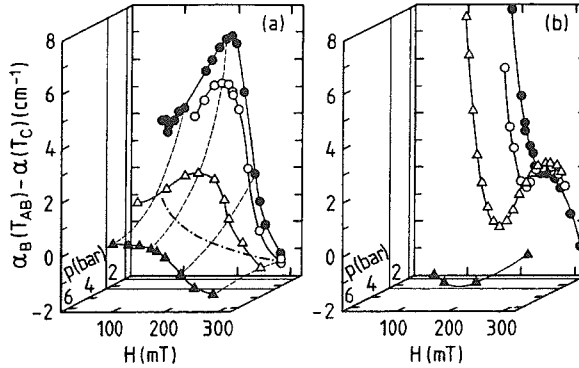


**Figure 12.** Sound attenuation  $\alpha_B(T_{AB}) - \alpha(T_C)$  vs. the magnetic field  $H$  and pressure  $p$  in  $^3\text{He-B}$  at  $T_{AB}$  [P4,70]. Note that temperature changes along the  $H$ -axis. The filled circles correspond to  $p = 0$ , open circles to  $p = 0.5$  bar, open triangles to  $p = 2.3$  bar, and filled triangles to  $p = 6.6$  bar, respectively. The solid and dashed lines are guides for the eyes. In (a)  $f = 8.9$  MHz; the dash-dotted curve shows  $\alpha$  measured at  $H = 0$  as a function of  $T_{AB}(H)$  at zero pressure, indicating that the observed anomalies originate from the magnetic field and not from temperature through the field-dependence of  $T_{AB}$ . In (b)  $f = 26.8$  MHz.

tion of  $\mathbf{H}$ , so that the attenuation component  $\alpha_{\parallel}$  is relevant. For  $f = 8.9$  MHz (Fig. 12a) there is a maximum and for  $f = 26.8$  MHz (Fig. 12b) a minimum at  $H \approx 200$  mT, independent of pressure. Furthermore, the rotation response of  $\alpha$  with  $f = 8.9$  MHz has an anomalously strong field dependence between 200 and 240 mT.

Our data have been interpreted qualitatively in terms of theoretical considerations of Ashida and Nagai [86]. They showed that according to the weak-coupling theory, which should best be valid at low pressures, the nature of the AB-transition changes at a critical field  $H_c$ . At zero pressure,  $H_c \approx 230$  mT which is very near the field where we observe the anomalous behavior. However,  $H_c$  should increase with pressure to 340 mT at  $p = 6.6$  bar. Above  $H_c$  the AB-transition is of first order: the B-phase energy gap (Eq. (4)) with a finite minimum  $\Delta_{\parallel}$  jumps discontinuously into the A-phase gap with nodes. Below  $H_c$  a second order transition is expected: The minimum of the B-phase energy gap should go continuously to zero when  $T_{AB}$  is approached. Because of strong-coupling effects, the AB-transition is possibly always of first order, but at low pressures it should be "almost" of second order when  $H < H_c$ :  $\Delta_{\parallel}(T_{AB})/\Delta_{\perp}(T_{AB}) \ll 1$ .

The sharp rise in attenuation in Fig. 12a when  $H$  decreases from 250 to 200 mT can now be explained by a fast drop in  $\Delta_{\parallel}(T_{AB})$  in this field range. The attenuation maxima in Figs. 12a and 12b could be caused by some resonances near the pair-breaking condition  $hf = 2\Delta_{\parallel}$ . However, such a peak should also be observed in a temperature sweep at  $H < 200$  mT because in that case  $2\Delta_{\parallel}(T) > hf$  at low temperatures, but  $2\Delta_{\parallel}(T_{AB}) < hf$ . A peak was not observed: at  $H < 200$  mT the attenuation increases monotonically when temperature is swept up until  $T_{AB}$  is reached. To summarize, the anomalous field dependence is very probably caused by the strong field dependence of  $H_c$  near  $\Delta_{\parallel}(T_{AB})$ , as discussed by Ashida and Nagai [86]. A quantitative analysis of our data could not be performed, because sound attenuation in the

field-distorted  $^3\text{He-B}$  near the AB-transition has not been calculated theoretically and because the calculations by Ashida and Nagai were not extended to account for the strong-coupling effects.

The second observation reported in Publication [P3] was a region of excess attenuation when the AB phase boundary was slowly driven through the cell. Our original speculative suggestion was that the effect would be caused by a layer of some intermediate phase between  $^3\text{He-A}$  and  $^3\text{He-B}$ . However, it turned out later that the data can, at least partly, be explained in a less exotic manner, namely by the different sound velocities in  $^3\text{He-A}$  and  $^3\text{He-B}$ . When the AB boundary is not parallel to the ultrasound crystals, the phase of the received sound wave depends on its position on the receiver crystal, because the sound rays in different parts of the cell have travelled different lengths in the  $^3\text{He-A}$  and in the  $^3\text{He-B}$ . Thus cancellation of signal takes place (see Section 2.2.3) and the apparent attenuation increases.

### 2.3.3. Real squashing mode under rotation

In magnetic fields below about 50 mT, the energy gap of  $^3\text{He-B}$  is almost isotropic. This means that the propagation of ultrasound has no angular dependence outside the collective modes, and no rotation response can be detected. However, this is not the case near the rsq-resonance: the strength of the coupling between ultrasound and the  $m_J$ -substates of the real squashing mode depends on the angle  $\gamma$  between  $\mathbf{q}$  and  $\hat{\mathbf{h}}$  (see Section 1.3.2). When dispersion is not taken into account, the coupling is proportional to the square of the spherical harmonics of rank 2,  $|\gamma_2^{m_J}(\gamma)|^2$  [51]. Only the substate with  $m_J = 0$  couples to ultrasound when  $\mathbf{q} \parallel \hat{\mathbf{h}}$ . In our setup  $\mathbf{q} \parallel \mathbf{H} \parallel \Omega$  where  $\Omega$  is the angular velocity of rotation. In the stationary state  $\hat{\mathbf{h}}$  is aligned with  $\mathbf{q}$  owing to the magnetic field; only the  $m_J = 0$  mode is excited, except near the walls of the chamber where  $\hat{\mathbf{h}}$  deviates from the direction of  $\mathbf{H}$ . Rotation tilts the effective magnetic field  $\hat{\mathbf{h}}$  away from the direction of the applied field, as discussed in Section 2.3.1, so that under rotation all five rsq-submodes can couple to ultrasound [P5,P6].

Figure 13 shows an rsq-spectrum measured in an axial field of 25 mT while the cryostat was rotated at 4 rad/s. The frequency of ultrasound was kept constant, at  $f = 62.5$  MHz, but temperature and thus the mode frequencies – which depend on  $\Delta(T)$  (see Eq. (13)) – were swept. Many of our main observations can be seen in this single spectrum. Firstly, all five rsq-submodes couple to ultrasound under rotation, even when  $\mathbf{H} \parallel \mathbf{q}$ . They produce attenua-

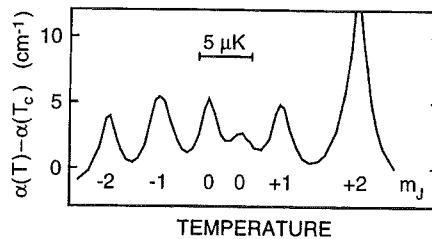


**Figure 13.** Ultrasound spectrum at  $f = 62.5$  MHz near the rsq-mode, obtained while the sample was rotated at  $\Omega = 4$  rad/s;  $p = 6.5$  bar,  $H = 25$  mT, and  $\mathbf{H} \parallel \Omega \parallel \mathbf{q}$  [P5,69].

tion maxima at temperatures where  $\omega_{\text{rsq},m_j}(T) = 2\pi f$ . Secondly, there are not five but six peaks: the  $m_j = 0$  resonance has split into a doublet [56,87] because it has a different frequency in the center of the cell where  $\hat{\mathbf{h}} \parallel \mathbf{H}$  and  $\hat{\mathbf{q}} \cdot \hat{\mathbf{h}} = 1$ , and near the walls where  $\hat{\mathbf{q}} \cdot \hat{\mathbf{h}} \approx 0$  because of the orienting effect of superflow (see Eq. (13)). Thirdly, there is an asymmetry between the heights of the peaks with positive and negative  $m_j$ , whereas  $|\gamma_2^{m_j}(\gamma)|^2$  depends only on the absolute value of  $m_j$  and not on its sign. This result was explained very satisfactorily by a phenomenological model, which takes dispersion effects into account [52].

In the experiments at  $p = 3.2$  bar, we observed two states of rotating  $^3\text{He-B}$ , which were characterized by clearly distinct and reproducible rsq-spectra. One of them, the V-state, was always obtained when the sample was cooled from above  $T_c$  down to the resonance temperature of the rsq-mode under continuous rotation. The second state, VF, formed normally when rotation was started in the superfluid state. The side peaks of the rsq-spectra in the VF-state were much stronger than in the V-state. Quite often, however, a VVF-spectrum, which was irreproducible but quite similar to the V-spectrum, was observed when rotation was started below  $T_c$ . Whether a VF- or a VVF-state was formed seemed to be almost entirely a matter of chance.

We identified V as a state with an equilibrium number of vortices and VF as the vortex-free state. The VF-state persisted up to velocities  $\Omega > 2.5$  rad/s, which is an unexpectedly large value for a vortex-free sample in our geometry. Even though the quartz wall of the chamber is very smooth one would expect that the  $1 \times 1$  mm<sup>2</sup> square filling holes (see Fig. 7a) act effectively as nucleation centers for vortices. Moreover, our later experiments in field-distorted  $^3\text{He-B}$  [P4] (see Section 2.3.1) indicated that at high fields the critical velocity for the creation of vortices in our chamber is only 0.2 rad/s. Thus the identification of VF as a vortex-free and V as the vortex state is by no means clear, even though no alternative explanation has been found.

According to Sauls and Serene [88], ultrasound can couple to the real squashing mode in a linear process even in the case of exact particle-hole symmetry, if there is a counterflow  $\mathbf{w} = \mathbf{v}_s - \mathbf{v}_n$  between the normal and superfluid components. The magnitude of coupling should be proportional to  $w^2$ . Salomaa and Volovik [52] suggested, as a direct experimental indication of this new coupling mechanism, a "gyrosonic effect": the rsq-spectrum should change when the relative direction between  $\Omega$  and  $\mathbf{q}$  is reversed. We did not detect any change in the attenuation traces when the sense of rotation was altered [P6]. Our noise level was below the expected magnitude of the gyrosonic effect, if a vortex-free state was assumed present in the chamber. However, the validity of this assumption is not clear, as was discussed previously. In the vortex state, where the average counterflow velocity is much smaller than in the absence of vortices, the gyrosonic effect could not have been observed.

The heights of the rsq-peaks changed by about 30% when the direction of sound propagation was altered. The explanation is that the energy of the transmitted sound pulses was more than an order of magnitude larger in one direction than in the other. A decrease in the height of the rsq-peak with increasing acoustic power has been observed earlier [61].

## 2.4. Nonlinear acoustics in $^3\text{He-B}$

### 2.4.1. Observation of two-phonon absorption by the real squashing mode

As discussed in Section 1.3.3, the approximate particle-hole symmetry of liquid  $^3\text{He}$  does not prevent the excitation of the real squashing mode in two-phonon processes. However, high acoustic intensities are required to produce such nonlinear phenomena: McKenzie and Sauls [66] showed that energy densities on the order of 10% of the superfluid condensation energy density  $U_c \sim 0.1 \text{ J/m}^3$  (Eq. (16)) are needed to make two-phonon absorption (TPA) by the rsq-mode detectable.

We observed TPA first in our cylindrical cell at zero pressure, driving one of the quartz crystals simultaneously by two 12- $\mu\text{s}$  rf-pulses [P7,P9,79,89]. Two parallel overlapping sound waves were thus produced: the signal wave of frequency  $f_s = 26.8 \text{ MHz}$  and the pump wave at  $f_p = 8.9 \text{ MHz}$ . The attenuation of the signal wave was measured, while the intense pump wave with energy density  $U_p \gtrsim 0.1 U_c$  was responsible for parametric excitation. Figure 14 shows the attenuation spectra of the signal wave at three different energy levels of the pump pulses. The larger peak, which becomes higher with increasing  $U_p$ , is caused by two-phonon absorption with parallel signal and pump pulses. A signal phonon and a pump phonon together excite the rsq-mode at temperature  $T_+ \approx 0.72 T_c$  where  $\omega_{\text{rsq},0}(T_+)/2\pi = f_s + f_p = 35.7 \text{ MHz}$  (see Eq. (14)). The satellite corresponds to TPA with antiparallel sound pulses [90], as will be discussed later. In both cases, only the  $m = 0$  submode couples with ultrasound.

Two-phonon absorption by the rsq-mode was observed under several experimental conditions, for pressures up to 3.5 bar, both in the cylindrical and in the cubic cells. The measured and calculated locations  $T_+$  for the main attenuation peak with parallel sound waves are summarized in Table I. The theoretical TPA-temperatures, obtained by putting  $\omega_{\text{rsq},0}(T_+)/2\pi = f_s + f_p$  in Eq. (14), somewhat depend on the choice of the constant  $a_{\text{rsq}}$  in the definition of

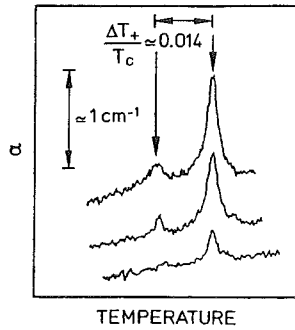


**Figure 14.** Two-phonon absorption by the real squashing mode at  $p = 0$  and  $H = 0$  [P7,79]. Attenuation spectra of the  $f_s = 26.8 \text{ MHz}$  signal wave in the presence of a pump wave with  $f_p = 8.9 \text{ MHz}$  are plotted for three different energies  $E_p$  of the 12- $\mu\text{s}$  pump pulses. From top to bottom:  $E_p = 1.5, 1.0$ , and  $0.3 \text{ nJ}$ , corresponding to energy densities  $U_p/U_c = 0.25, 0.17$ , and  $0.05$ , respectively. The pulse energy of the signal wave is  $E_s = 0.06 \text{ nJ}$  in all cases, i.e.,  $U_s/U_c = 0.01$ . The larger attenuation peak is located at  $T_+/T_c \approx 0.72$ .

**Table I.** Comparison of the experimentally measured temperature  $T_+$  with the theoretically calculated values for the main TPA peak for  $\mathbf{q}_s \parallel \mathbf{q}_p$  at  $H = 0$ . The calculated results were obtained from Eq. (14) with  $v_0^2 = 0.442 v_F^2$ , and using two different values for  $a_{\text{rsq}}^2 = \hbar \omega_{00} / \Delta(T)$ .

$p$ (bar)	$f_s$ (MHz)	$f_p$ (MHz)	$T_+/T_c$ (calculated)		$T_+/T_c$ (measured)
			$a_{\text{rsq}}^2 = 1.60$	$a_{\text{rsq}}^2 = 1.43$	
0	26.8	8.9	0.721	0.672	$0.72 \pm 0.02$
2.7	44.7	8.9	0.606	0.504	$0.56 \pm 0.03$
2.7	26.8	26.8	0.606	0.504	$0.54 \pm 0.02$
3.5	44.7	8.9	0.676	0.611	$0.64 \pm 0.02$
0	15.1	5.0	0.927	0.918	$0.93 \pm 0.02$
0	25.15	15.1	0.593	0.482	$0.53 \pm 0.02$
2.0	25.15	15.1	0.791	0.759	$0.75 \pm 0.03$

$\omega_{00}$  (see below Eq. (13)). Two values were used in Table I:  $a_{\text{rsq}}^2 = 1.60$  comes from the BCS weak-coupling theory without Fermi-liquid and higher-order pairing corrections [6], whereas the value  $a_{\text{rsq}}^2 = 1.43$  was obtained from earlier experiments in the linear region [39,91]. The locations  $T_+$  of the observed attenuation peaks are in reasonable agreement with the positions expected for TPA. Table I shows that two-phonon absorption occurred also for  $f_s = f_p$ . One sound pulse, with frequency  $f = 26.8$  MHz and energy density  $U \simeq 0.02 U_c$ , was transmitted at a time, without applying a separate pump wave. Two-phonon absorption took place at  $T_+$  where  $\omega_{\text{rsq},0}(T_+)/2\pi = 2f$ ; a satellite peak was observed as well.

The dependence of the height  $\Delta\alpha$  of the attenuation peak on the energy density of the pump wave, which can be clearly seen in Fig. 14, is typical for nonlinear processes. Eq. (17) predicts a linear relationship between  $\Delta\alpha$  and  $U_p$ , and this is approximately what was observed [P7,P9]. The absolute magnitudes of the attenuation maxima are in agreement with the prediction as well. However, there is one feature in our results which the calculation does not explain: the height of the TPA-peak depends not only on  $U_p$  but also on  $U_s$ , the energy density of the signal wave, even when  $U_s \ll U_p$ . We studied this systematically in our cubic cell. When  $U_s/U_c$  was decreased from 0.015 to 0.00015, keeping the pump level constant at  $U_p = 0.11 U_c$ , the height of the TPA maximum increased by more than a factor of 5. Simultaneously the peak became narrower so that its area remained approximately constant.

As mentioned earlier, the satellite on the low-temperature side of the main peak is caused by counterpropagating sound waves [90]: the pump pulse that had been reflected partly from the receiver crystal interacts with the incoming signal pulse, exciting the  $m = 0$  rsq-mode in a two-phonon process. Because of the conservation of momentum, the wave vector of the excited rsq-mode is given by  $\mathbf{q} = \mathbf{q}_s + \mathbf{q}_p$ , where  $\mathbf{q}_s$  and  $\mathbf{q}_p$  are the wave vectors of the signal



and pump pulses, respectively. When the waves are parallel,  $\mathbf{q}_s \uparrow \uparrow \mathbf{q}_p$ , the rsq-mode is excited with the wave number  $q^{\uparrow\uparrow} = q_s + q_p = 2\pi(f_s + f_p)/c$ , where  $c$  is the velocity of zero sound, but for counterpropagating waves with  $\mathbf{q}_s \uparrow \downarrow \mathbf{q}_p$  the wave number of the excited mode becomes  $q^{\uparrow\downarrow} = |q_s - q_p| = 2\pi|f_s - f_p|/c$ . The mode frequency is different in the two cases, according to the  $q$ -dependence of Eq. (14), so that in a constant-frequency experiment the rsq-mode is excited at a higher temperature when  $\mathbf{q}_s \uparrow \uparrow \mathbf{q}_p$  (main peak) than when  $\mathbf{q}_s \uparrow \downarrow \mathbf{q}_p$  (satellite).

The side peak was observed in most of the experimental conditions quoted in Table I. Its position and other properties are in such good agreement with the model of antiparallel waves that there is no doubt about the validity of this explanation, even though the side peak was in the cylindrical cell about 40% higher and in the cubic cell 50% lower than expected on the basis of simple arguments. It is interesting to note that in the case of TPA by a single-frequency sound wave, the side peak is caused by two phonons which move in opposite directions with the same wave number. Therefore, the excited real squashon has  $q = 0$ , i.e., its group velocity is zero and the effect of dispersion on the frequency of the mode is absent.

Our observation of the five-fold Zeeman splitting of the  $\uparrow\uparrow$ -resonance in a magnetic field perpendicular to the common direction of the signal and pump pulses is presented in Fig. 15. As in the linear case [51], it ultimately shows that our discovery is caused by the  $J = 2^+$  rsq-mode. The attenuation of an  $f_s = 25.15$  MHz signal wave was measured in the presence of a parallel  $f_p = 15.1$  MHz pump wave at  $p = 0$  in the cubic cell. At  $H = 0$ , Fig. 15a, the satellite peak ( $\uparrow\downarrow$ ), caused by the reflected pump wave, is again present. At  $H = 34.8$  mT, Fig. 15b, all the five  $m_J$ -substates of the main resonance with  $\mathbf{q}_s \uparrow \uparrow \mathbf{q}_p$  can be seen. Only the  $m_J = 0$  and  $m_J = \pm 2$  modes couple to ultrasound when  $\mathbf{q}_s \parallel \mathbf{q}_p \perp \mathbf{h}$ . The  $m_J = \pm 1$  submodes with  $\mathbf{q}_s \uparrow \uparrow \mathbf{q}_p$  are resolved, though weakly, because  $\mathbf{h}$  turns off the direction of applied magnetic field near the walls. The peaks with  $m_J > 0$  are clearly higher than those with  $m_J < 0$ , like in the linear case (see Fig. 13). In a perpendicular magnetic field all submodes of the  $\uparrow\downarrow$ -resonance are too weak to be observable.

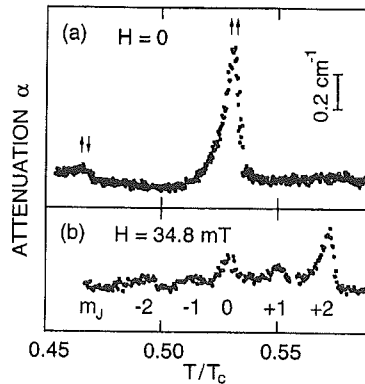


**Figure 15.** Five-fold Zeeman splitting of the main TPA-peak at zero pressure for  $\mathbf{q}_s \parallel \mathbf{q}_p$ , with  $f_s = 25.15$  MHz and  $f_p = 15.1$  MHz [P9]. (a) Attenuation spectrum in zero magnetic field, showing the main peak excited with  $\mathbf{q}_s \uparrow \uparrow \mathbf{q}_p$  and the satellite with  $\mathbf{q}_s \uparrow \downarrow \mathbf{q}_p$ . (b) Spectrum in a magnetic field of  $H = 34.8$  mT, applied perpendicular to the propagation of the sound waves.

### 2.4.2. Application of two-phonon absorption: dispersion in the rsq-mode

Multiwave resonances have remarkable advantages as probes of collective modes in  $^3\text{He-B}$ . When the signal and the pump waves are not parallel, substates with  $|m| \neq 0$  can couple to ultrasound even for  $H = 0$ , unlike in the linear case: direct observation of dispersion splitting of the rsq-mode in zero magnetic field is possible. Moreover, the wave number  $q$  and the frequency  $\omega_{\text{rsq}}$  of the excited mode can be altered independently, by changing the angle  $\theta$  between the signal wave vector  $\mathbf{q}_s$  and the pump wave vector  $\mathbf{q}_p$ : the wave number of the excited mode is given by  $q = |\mathbf{q}_s + \mathbf{q}_p| = (q_s^2 + q_p^2 + 2q_s q_p \cos \theta)^{1/2}$ , but the angular frequency is always  $\omega_{\text{rsq}} = 2\pi(f_s + f_p)$ , independent of  $\theta$ . Therefore, it is possible to measure directly the dispersion relation  $\omega_{\text{rsq}} = \omega_{\text{rsq}}(q)$ . In one-phonon studies the collective modes can only be excited along one line in the  $q$ - $\omega$  plane: that defined by the dispersion relation of ultrasound,  $\omega = cq$  (see Fig. 4b).

In our cubic cell, the signal and the pump pulses could be transmitted both parallel ( $\mathbf{q}_s \uparrow \uparrow \mathbf{q}_p$ ) and perpendicular ( $\mathbf{q}_s \perp \mathbf{q}_p$ ) to each other. A third relative orientation was obtained in the former case near the receiver crystal, where the two waves were partially antiparallel ( $\mathbf{q}_s \uparrow \downarrow \mathbf{q}_p$ ) because of the reflection of the pump wave, as discussed in Section 2.4.1. Figs. 16a and 16b show two spectra measured in the absence of a magnetic field at zero pressure, with  $f_s = 25.15$  MHz and  $f_p = 15.1$  MHz, applying the pump and signal pulses in the parallel (a) and perpendicular (b) directions. The large peak at  $T_0^{\uparrow\uparrow}/T_c = 0.53$  in Fig. 16a is

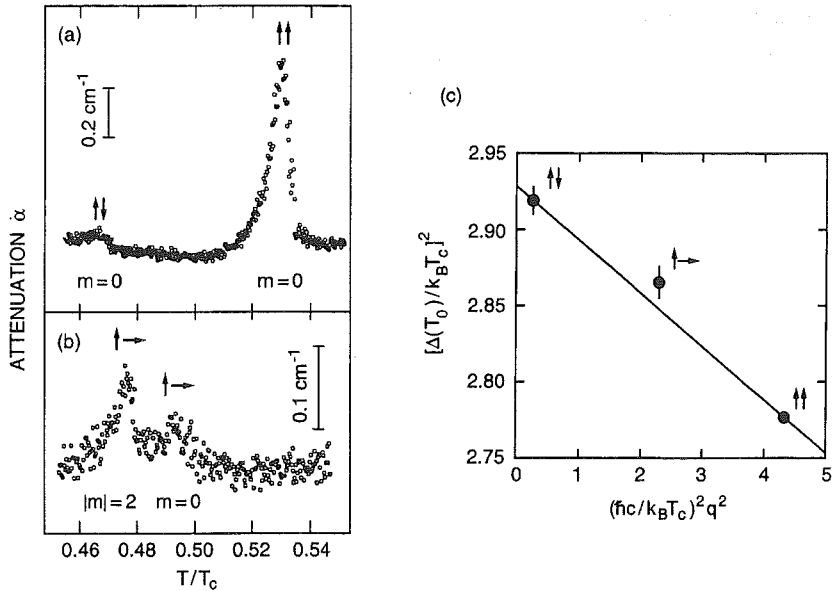


**Figure 16.** Attenuation spectra of an  $f_s = 25.15$  MHz signal wave in the presence of an  $f_p = 15.1$  MHz pump wave at  $p = 0$ ,  $H = 0$ , for (a)  $\mathbf{q}_s \parallel \mathbf{q}_p$  and (b)  $\mathbf{q}_s \perp \mathbf{q}_p$  [P8]. (c) The square of the BCS gap function  $[\Delta(T)]^2$  at the temperature of TPA for the  $m = 0$  substate with different relative orientations of  $\mathbf{q}_s$  and  $\mathbf{q}_p$ , as a function of  $q^2 = |\mathbf{q}_s + \mathbf{q}_p|^2$ .  $[\Delta(T)]^2$  is scaled by  $(k_B T_c)^2$  and  $q^2$  by  $(\hbar c / k_B T_c)^2$ . A linear relationship between  $[\Delta(T)]^2$  and  $q^2$  is expected.

due to two-phonon absorption by the  $m = 0$  rsq-mode with  $\mathbf{q}_s \uparrow\uparrow \mathbf{q}_p$ . The same mode, excited by antiparallel waves (reflection), produces the side peak at  $T_0^{\uparrow\downarrow}/T_c = 0.466$ . Only the  $m = 0$  substate is excited when  $\mathbf{q}_s \uparrow\uparrow \mathbf{q}_p$  or  $\mathbf{q}_s \uparrow\downarrow \mathbf{q}_p$ . In the lower spectrum, Fig. 16b, the two peaks arise from the dispersion splitting of the rsq-mode: the submodes with  $m = 0$  and  $|m| = 2$  couple to ultrasound when  $\mathbf{q}_s \perp \mathbf{q}_p$ , producing attenuation maxima at  $T_0^{\perp}/T_c = 0.493$  and at  $T_2^{\perp}/T_c = 0.477$ , respectively.

From the locations of the attenuation maxima, experimental values for the dispersion coefficients  $c_a^2$  and  $c_b^2$  in Eqs. (13) and (14) can be extracted. The results are  $c_a^2 = (0.30 \pm 0.07)v_F^2$  and  $c_b^2 = (0.30 \pm 0.06)v_F^2$ , which should be compared with theoretical values  $c_a^2 = 0.224v_F^2$  and  $c_b^2 = 0.327v_F^2$  [53]. This was the first measurement of  $c_a^2$ . The value of  $c_b^2$  has been deduced earlier from two experiments [56,92], and the results are in agreement with the present data.

Using different relative orientations between the signal and the pump pulses, the substate with  $m = 0$  could be excited with three different wave numbers,  $q_s - q_p$  ( $\uparrow\downarrow$ ),  $(q_s^2 + q_p^2)^{1/2}$  ( $\perp$ ), and  $q_s + q_p$  ( $\uparrow\uparrow$ ), keeping its frequency constant. In Fig. 16c,  $\Delta(T)^2$  at the peak position has been plotted against  $q^2$ . Our results confirm, at least approximately, the linear relationship between  $\Delta(T)^2$  and  $q^2$ , which is predicted by Eq. (14) with  $\omega_{\text{rsq},0} = 2\pi(f_s + f_p) = \text{constant}$  and  $\omega_{00} = a_{\text{rsq}}\Delta(T)/\hbar$ . However, the datum measured with perpendicular pulses lies slightly above the line that goes through the two outermost points. A small curvature in the plot of  $\Delta(T)^2$  vs.  $q^2$  is, in principle, allowed by theory when higher-order terms are included in Eq. (14), but the error bars in Fig. 16c are too long to allow clear conclusions to be made about the magnitude of such higher-order effects.

### 2.4.3. Two-phonon pair-breaking edge

When only one sound wave with frequency  $f$  was transmitted through the sample at a time, nonlinear phenomena were detected near the two-phonon pair-breaking edge, where  $\Delta(T) = hf$  [P9]. At this temperature the energy of the two phonons is just enough to excite both members of a Cooper pair over the energy gap:  $2hf = 2\Delta(T)$ . We studied the observed anomaly as a function of acoustic intensity and magnetic field. Similar studies have been performed by Peters and Eska [93] in the absence of a magnetic field.

Most of our experiments were done at zero pressure in the cylindrical cell, with  $f = 26.8$  MHz. The energy density  $U/U_c = 0.002$  was already large enough to produce a clearly observable step in the attenuation spectrum at  $T/T_c \approx 0.76$ . Within the accuracy of our thermometry, about  $\pm 0.02T_c$ , this temperature matches with the expected location of the two-phonon pair-breaking edge:  $hf = \Delta(T)$  at  $T/T_c \approx 0.74$ . When the energy density of the sound pulses was increased, in the absence of magnetic field, from  $0.002U_c$  to  $0.06U_c$ , the step increased by about  $2.5 \text{ cm}^{-1}$ . Another consequence of higher sound intensity was that a new peak developed at the edge of the step. It could be seen as an anomaly in the phase-velocity spectra as well (see the lowest traces in Figs. 17a and 17b). The origin of the peak is unknown, but the step is probably caused by two-phonon pair-breaking, which becomes possible when  $hf \geq \Delta(T)$ .

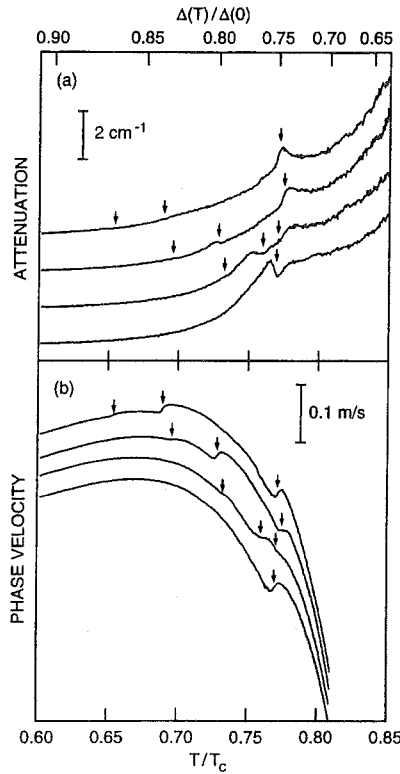


**Figure 17.** (a) Attenuation and (b) phase velocity of ultrasound pulses with  $f = 26.8$  MHz and  $U/U_c = 0.06$  near the two-phonon pair-breaking edge at zero pressure in different magnetic fields [P9]. From bottom to top,  $H = 0, 34.8, 63.8,$  and  $88.2$  mT; the field was applied parallel to the direction of ultrasound propagation. The positions of the anomalies in the phase velocity spectra (b), identified by arrows, are marked by similar arrows on the corresponding attenuation traces (a).

In an applied magnetic field ultrasound response displays even more structure near the two-phonon pair-breaking edge. The attenuation and phase-velocity spectra of  $f = 26.8$  MHz ultrasound in several fields between 0 and 88.2 mT are presented in Fig. 17. The field was applied parallel to the propagation direction of the sound pulses, and the energy density of ultrasound was  $U/U_c = 0.06$ . The evolution of the  $hf = \Delta$  anomaly is best seen in the phase velocity spectra of Fig. 17b: the single feature observed at  $H = 0$  is split into a triplet by the magnetic field. Only some of the features are detectable in the attenuation spectra of Fig. 17a, where the positions of the phase velocity anomalies are shown by small arrows. One notes, however, that the attenuation peak observed at  $H = 0$  weakens with increasing field and shifts to a lower temperature, and an attenuation maximum develops near  $T/T_c = 0.76$ . When the cryostat was rotated in an 88.2-mT field, the attenuation peak was smoothed out and the anomalies in phase velocity disappeared. An external field applied perpendicular to the sound propagation axis removed the anomaly in the phase velocity as well; this was observed in our cubic cell.

There are no theoretical predictions about two-phonon processes near the pair-breaking threshold, so the interpretation of our results is quite speculative. However, the  $H$ -dependence of the weak lowest-temperature feature in Fig. 17b is very similar to that of the effective pair-breaking edge, when both the distortion of the gap and the Zeeman splitting of the quasiparticle states are taken into account [47,94]. Furthermore, one of the features may be caused by the  $J = 0^+$  "real gap mode", which is expected to couple to ultrasound in two-phonon processes.

### 3. Optical experiments

The original impetus for starting optical experiments on superfluid  $^3\text{He}$  was the hope that the vortex lattice could possibly be seen directly by looking at the free surface of rotating  $^3\text{He-B}$ : each vortex produces a dimple on the surface [95,96]. However, it soon turned out that the dimples are too small to be observable by conventional optical methods; their predicted depth is only about 1 nm [P12], i.e., almost three orders of magnitude smaller than the optical wavelength. There exist special optical techniques with which even so tiny objects can be detected, but their application inside the cryostat would be extremely difficult and far beyond the scope of this thesis. Nevertheless, we decided to start testing methods which would allow visual observations of superfluid  $^3\text{He}$ . We considered it challenging enough to develop a totally new technique for experiments below 1 mK. Our concrete aim was to repeat, in the case of  $^3\text{He}$ , Osborne's experiment [15] in which he detected the parabolic meniscus of rotating superfluid  $^4\text{He}$ . In addition to investigations of the free surface of a rotating superfluid, there are very interesting further applications for optics in studies of crystallization of  $^3\text{He}$  at ultralow temperatures.

#### 3.1. Experimental techniques

##### 3.1.1. Preliminary tests of optics at low temperatures

Before this work, optical imaging experiments at low temperatures have been performed using optical cryostats, in which the sample is studied from room temperature through several windows (see, however, Ref. [19]). Because the windows also let in some of the 300-K blackbody radiation, the minimum temperature in those experiments was limited to several tens of millikelvins [97]. To study the free surface of superfluid  $^3\text{He}$ , one has to cool to almost two orders of magnitude lower: below 0.93 mK. Obviously, a new way for performing the experiments is required. The results of this thesis demonstrate that by using optical fibers instead of windows to transmit light between room temperature and the sample, optical investigations are possible at submillikelvin temperatures. Fibers have been used previously in the "pseudo-optical" experiments by Williams and Packard [19] to transmit light from a phosphor screen at low temperature ( $T \simeq 0.1$  K) to a camera at room temperature.

Before the measurements were ready to be started in the ROTA2-cryostat, we investigated experimentally the feasibility of optical photography at ultralow temperatures. A small dilution refrigerator, built just for this purpose, was used to test the properties of optical mate-

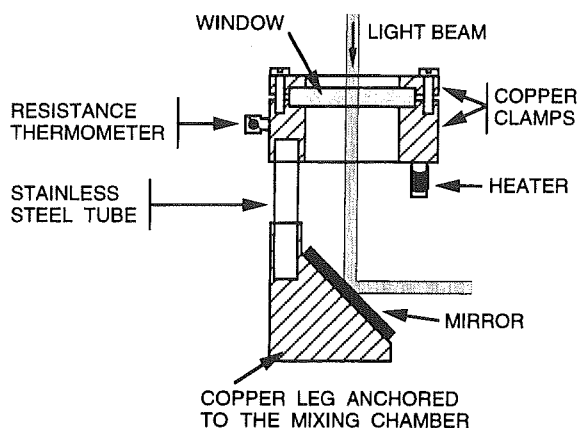


**Figure 18.** Construction of the calorimeter which was used to measure the absorption of light into several window materials.

rials at low temperatures. The first prototype of a complete system to study the free liquid surface was tested as well.

Absorption of light by several window materials was measured with a calorimeter whose construction is shown in Fig. 18. The window was clamped between two annular copper parts, connected to the mixing chamber of the dilution refrigerator by a weak thermal contact which was made of a 10 mm long stainless steel tube of 4 mm diameter and with 0.2 mm wall thickness. Light was transmitted from a He-Ne laser at room temperature into the cryostat through a single-mode optical quartz fiber and collimated into a beam of about 2-mm diameter. The light was conducted through the window under study and then via a mirror and through a hole in the radiation shield onto the black-painted inner surface of the vacuum jacket. When light was let into the cryostat, part of it was absorbed by the window, heating the copper clamps. The increase in temperature was recorded with a 68- $\Omega$  Matsushita resistance thermometer (see Fig. 18). The absorbed light power was determined by measuring how much power had to be fed into a resistive heater, which was thermally connected to the clamps, in order to cause the same increase in temperature as the shining of light. The total light power was measured in a similar way, but using a black-painted copper disk instead of the window.

Three materials were tested: the conventional optical borosilicate crown glass BK7, sapphire, and fused silica (Herasil, manufactured by Heraeus Quartzglas GmbH, Hanau, Germany). The results are collected in Table II. The thickness of every sample was 3 mm, the total power of the light beam was 20  $\mu$ W, and the measurements were performed at  $T \approx 100$  mK. Absorption by BK7 was clearly larger than by the other two materials. The same result was obtained during three different cooldowns, between which the window was cleaned, so that we believe absorption into the BK7 material itself was recorded. However, one should note that our measurements gave about two orders of magnitude larger absorption coefficients than the room-temperature values quoted by the supplier (Optics Guide 5, Melles Griot Inc., Irvine, California) for both BK7 and fused silica. The measured absorption of the sapphire

**Table II.** Absorption of red light by three window materials at  $T \simeq 100$  mK. The relative accuracy of the results is about  $\pm 50\%$ . The measured absorption can be caused partially by impurities on the surfaces of the windows, etc., especially for sapphire and fused silica.

Material	Absorption ( $\text{mm}^{-1}$ )
BK7	$8 \cdot 10^{-3}$
Sapphire	$1 \cdot 10^{-3}$
Fused silica	$3 \cdot 10^{-4}$

and fused silica windows can be caused partly by impurities on their surfaces. Heating by stray light, measured with no window in the calorimeter, was smaller than but of the same order of magnitude as absorption into fused silica. Based on these results, fused silica was chosen as the window material in our experiments [P11].

We also tested the possibility of using a charge coupled device (CCD) sensor, located inside the vacuum jacket of the cryostat, for the detection of light. One of the problems encountered with this is that silicon-based CCD does not work at very low temperatures: it has to be kept above 50 ... 60 K. Thermal radiation from the sensor has to be blocked by a suitable filter, which is transparent for visible light but absorbs blackbody radiation at long wavelengths. We measured the radiation heat leak from the CCD sensor using a calorimeter similar to that depicted in Fig. 18, but with a  $1\text{-cm}^2$  black surface in place of the window. The CCD sensor, whose package had an area of  $5\text{ cm}^2$ , was located 20 cm above the calorimeter and heated to 60 K. Radiation from the sensor into the calorimeter was exposed through a 10-mm diameter filter window, which was mounted on the still plate about 10 cm above the calorimeter, at  $T = 0.8$  K.

An 8-mm thick  $\text{CaF}_2$  window alone was not a sufficient filter: 30 nW of thermal radiation from the CCD sensor went through it into the calorimeter. When a 3-mm thick sapphire window was added, the heat leak was reduced to about 5 nW, which is still quite large but tolerable. One more suitable filter material would be BK7 [72]. It is important to use different materials as filters: if one of the windows transmits a band at long wavelengths, the other can absorb it. A part of the measured heat load can be caused by stray radiation through small holes in the still plate. One should note that we could not perform these experiments while the CCD was on, owing to electrical noise problems. Instead, the sensor was heated externally to 60 K. According to our other measurements, CCD works when the package is at this temperature or above. However, it may be that the silicon chip of an operating sensor is at somewhat higher temperature than the package, in which case the radiation heat leak would be larger than what we measured.

Our first prototype of the complete system to study the surface of liquid  $^3\text{He}$  was tested in the small cryostat. The construction was quite similar to our final setup (see Fig. 19a). Illumination entered from room temperature into the cold parts through an optical fiber. The

light beam was conducted via a beam splitter and lenses directly from above into the sample cell with transparent top and bottom windows. The light reflected from the bottom window was monitored by a video camera (Philips LHD 0461/02). Its CCD sensor chip (Philips NXA1011) was located inside the vacuum jacket and heated to  $T \approx 60$  K. The other parts of the camera were at room temperature, connected electrically to the sensor by wires 1.5 m long. The sensor that we used was not very suitable for such remote operation. Its output was divided into three separate registers, and their signals interfered with each other causing stripes into the picture.

The free surface of liquid  $^3\text{He}$  in the partially filled cell could be detected indirectly: the light beam expanded and became distorted because of refraction at the liquid surface before and after reflection from the bottom window. The surface of  $^3\text{He}$  was curved because of capillary rise on the cylindrical wall of the cell, whose diameter was only 7 mm. We could not see the interference pattern produced by light reflected from the fluid surface or from the bottom window of the cell, because the sample was vibrating too much. The cell was thermally anchored to the mixing chamber of the refrigerator, and its temperature was about 100 mK during illumination. At such high temperatures the viscosity of  $^3\text{He}$  is too small to effectively damp the surface oscillations.

### 3.1.2. Optical apparatus in ROTA2

A schematic view of the experimental setup that was used in our optical experiments in the ROTA2-cryostat is presented in Fig. 19a [P11]. The main difference between this apparatus and the one that was tested in the small cryostat is that now the CCD sensor is not inside the vacuum jacket of the cryostat. Instead, the whole video camera is at room temperature, and light is conducted up to 300 K through a coherent bundle of optical fibers.

Referring to Fig. 19a, the source of illumination LA is a 5-mW He-Ne laser (LC5L, Limab, Gothenburg, Sweden) which rotates with the cryostat and operates at room temperature. The light beam is coupled by a microscope objective into a single-mode optical step-index quartz fiber F (Semiconductor Laboratory, Technical Research Centre of Finland, Espoo, Finland), which conducts illumination into the cold parts of the apparatus. Light that enters the cryostat is first collimated by the convex lens L3 to a parallel beam of 2 mm diameter. It is then guided into the partially filled sample cell OC via a beam splitter and two mirrors, M1 and M2. The diameter of the parallel beam is expanded to 10 mm by two plano-convex fused silica lenses L1 and L2, which are 300 mm apart and have focal lengths  $f_1 = 50$  mm and  $f_2 = 250$  mm, respectively.

Light reflected from the bottom window WW of the cell OC or from the free surface of the  $^3\text{He}$  sample S is conducted via L2, M2, M1, L1 and BS into the lower end of FB, a 2.2-mm-diam coherent bundle of 30000 optical fibers (Mitsubishi Cable Inc., Japan). Light then passes through FB to room temperature, where it is detected by the video camera CCD (Philips LHD 0461/02), focused to the upper end of FB by a positive lens L4. However, only a small fraction of light is reflected; more than 90% of the beam passes through the cell and is guided by a 45° mirror M3 through a hole in the inner radiation shield onto a black surface on



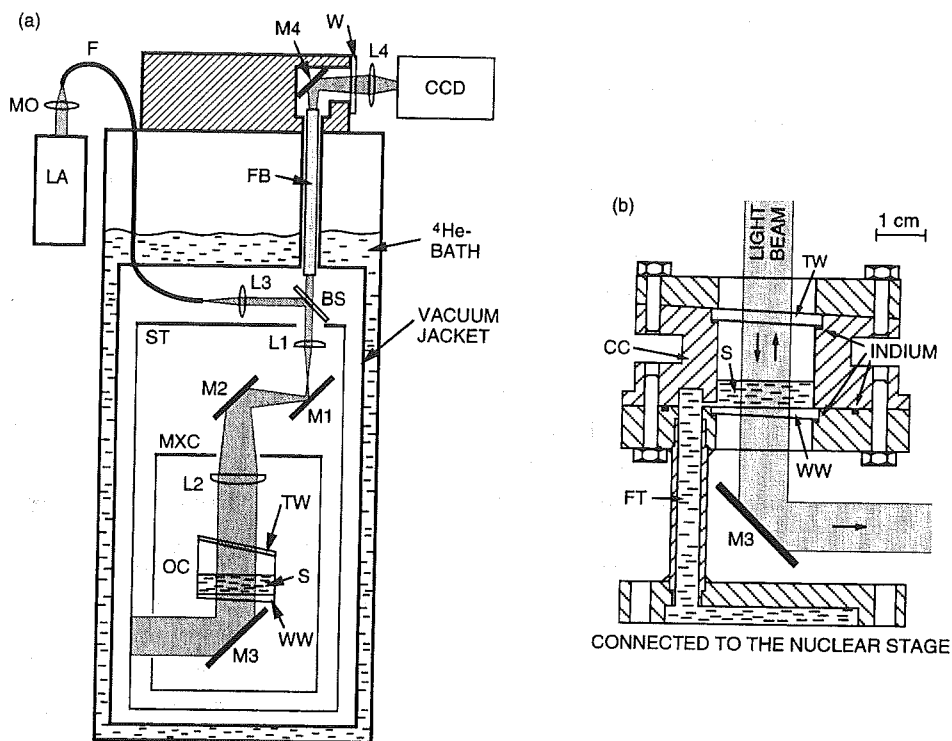


**Figure 19.** (a) Schematic illustration of the optical apparatus (not to scale) [P11], and (b) a close-up of the experimental chamber. Explanation of symbols: LA, laser; MO, microscope objective; F, optical fiber; L1 – L4, lenses; BS, beam splitter; M1 – M4, aluminium coated mirrors; OC, optical cell; TW, tilted top window; WW, wedged bottom window; S,  $^3\text{He}$  sample; ST, still of the dilution refrigerator; MXC, mixing chamber; FB, optical fiber bundle; W, window; CCD, video camera; CC, cylindrical copper wall of the experimental chamber; FT, filling tube.

the outer radiation shield, thermally anchored to the still ST of the dilution refrigerator. M3 hangs from the bottom of the mixing chamber MXC.

Construction of the optical cell OC is presented in Fig. 19b. The sample volume is formed by an annular copper part CC and by the top and bottom windows, TW and WW. All surfaces of the windows have been antireflection coated with  $\text{MgF}_2$ , so that their reflection coefficients are about 0.01. The top window TW is tilted by  $2^\circ$  and the bottom window WW wedged by the same amount, so that only reflection from the reference plane, i.e., the upper surface of WW, reaches the bottom of the fiber bundle FB and the video camera CCD. The windows are about 2-mm thick, and their material is fused silica (Herasil, manufactured by Heraeus Quartzglas GmbH, Hanau, Germany). The seals between the windows and the copper parts have been made using indium O-rings. The inner diameter of the sample volume is 20 mm. It has to be large since capillary forces on the walls of a smaller cell would disturb the surface profile too much [98]. The sample S is connected to the heat exchanger volume of the

nuclear stage (see Fig. 6) through a  $1 \times 1 \text{ mm}^2$  square hole just above the bottom window WW, and through a filling tube FT with an inner diameter of 4 mm.

The power of the light beam that reaches the cell is  $60 \text{ } \mu\text{W}$ , as was measured at room temperature with a photodiode. Continuous illumination causes a heat leak of about  $2 \text{ } \mu\text{W}$  into the nuclear stage, i.e., 3% of light is absorbed. According to Table II, less than 0.15% of light should be absorbed on the fused silica windows TW and WW whose total thickness is about 4.5 mm. Absorption into the sample itself is very small as well: no change in the heat leak was observed when the thickness of the  $^3\text{He}$ -layer in the cell was increased from 2 to 6 mm. Most probably the main heat leak due to illumination is caused by secondary reflections and scattered light. The sample is typically illuminated by 50-ms pulses every 5 seconds, so the average heat load is on the order of 20 nW. Thermometry is based on Pt-NMR, as discussed in Section 2.1 (see Fig. 6). The minimum temperature that was reached in our optical experiments was about 0.7 mK. The limit was not set by the optical apparatus but rather by a conductive heat leak into the thermometer probe through the wires of its rf-coil.

Figure 20a shows a typical video picture of reflection from the reference plane (the upper surface of WW) in a partially filled cell. Light reflected from the free liquid surface does not reach the camera in this case. The luminous circular part is the end of the fiber bundle FB, and it corresponds to a region with diameter of about 6 mm in the optical cell OC. The picture has some inhomogeneities, which are partially produced by aberrations in the optical components. However, the four clearest circular features, one of which is marked by an arrow, are

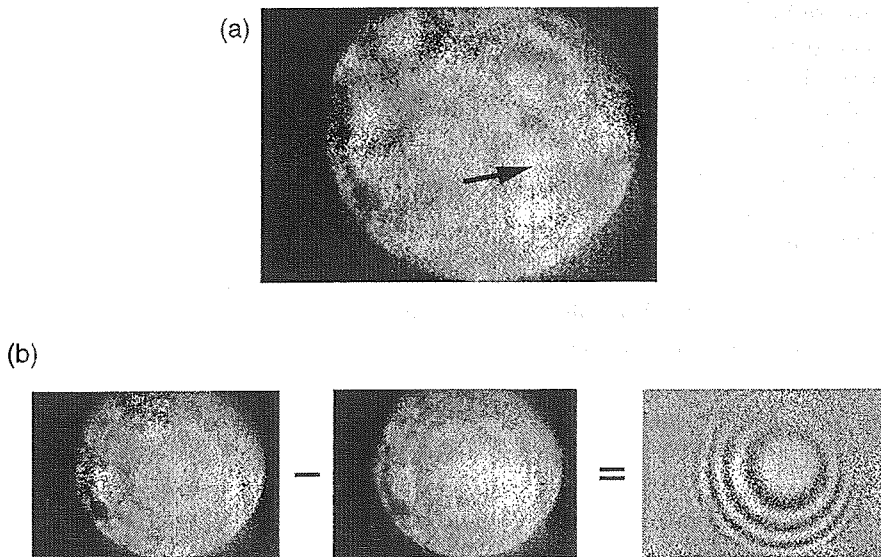


**Figure 20.** (a) A typical reflection from the bottom window of a partially filled cell. One of the four circular features caused by droplets of the liquid on the top window is indicated by the arrow. (b) First two frames: Interference patterns produced by light reflected from the bottom window of the cell and from the surface of liquid  $^3\text{He}$ . Third frame: Difference of the first two frames, taken 20 ms apart.

probably caused by droplets of  $^3\text{He}$  (or possibly  $^4\text{He}$ -impurities) condensed under the top window TW of the optical cell. They disappear when the cell is totally filled, so that the lower surface of TW is covered by liquid. The features can also be "boiled off" by illuminating the sample continuously for a few hours (see the first two frames in Fig. 20b), but within several days they form again at their original positions. The inhomogeneities of the picture were used as "markers" in some experiments [P11] (see Sections 3.2.1 and 3.2.2).

The first two frames of Fig. 20b are the video pictures received when the cryostat was adjusted so that the free surface of the sample was parallel to the reference plane. Reflection from both of these interfaces reached the lower end of FB and was detected by CCD. The two light beams form an interference pattern which is, however, only barely resolvable in the printed pictures. The contrast is weak because the difference in the intensities of the interfering beams is very large: the reflection coefficient of  $^3\text{He}$  is  $R_3 = 1.2 \cdot 10^{-4}$ , whereas that of the reference surface is almost two orders of magnitude larger,  $R_r \approx 0.01$  even after antireflection coating. Quantitatively, the contrast can be expressed as the ratio  $C$  of the intensity of the bright fringes, where the beams interfere constructively, and of the dark fringes, where the interference is destructive, i.e.,

$$C = 1 + \frac{4}{\sqrt{R_r/R_3} + \sqrt{R_3/R_r} - 2} \quad (25)$$

In our case one obtains  $C = 1.6$ .

Rotation of the cryostat (see Section 3.2.2) and the fountain effect in the superfluid state (see Section 3.2.3) cause temporal changes in the interference pattern, which can easily be seen on the video monitor. The contrast of interference can be improved by subtracting two video frames from each other, pixel by pixel, using a computer (public-domain program Image in Macintosh Quadra 700); the constant background disappears and only the changing features are left. The interference rings are very clear in the third frame of Fig. 20b, which is the difference of the first two pictures, taken 20 ms apart.

The circular fringes are present even when the cryostat is stationary, i.e., when the liquid surface is flat. They are formed because the upper surface of the bottom window WW, from which the other interfering beam reflects into the camera, is slightly convex; in order to seal the cell, WW had to be tightened so much that it was deformed. Between two dark rings, the thickness of the liquid layer above the curved window changes approximately by one half of optical wavelength,  $\lambda/2 = 316 \text{ nm}$ . This is not accurately valid in our setup for which, unlike for a conventional interferometer, the image of the reference plane is not formed on the bottom of the fiber bundle FB. The reason for such a construction is that before the experiments we could not be sure that the interference pattern is visible at all; in our tests in the small cryostat it was not. In the system depicted by Fig. 19, the curvature of the surface of  $^3\text{He}$  can be determined even in the absence of interference, from expansion of the beam which reflects from the bottom window of the cell and which is refracted by the liquid surface.

## 3.2. Experimental results

### 3.2.1. Superfluid transition

The rapid change in the viscosity of  $^3\text{He}$  at the superfluid transition can be *seen* directly, when the cryostat is rotated so that its axis is slightly tilted with respect to gravity. Below  $T_c$  the light beam reflected from the reference surface precesses with the frequency of rotation. This can be seen as a circular motion of the inhomogeneities in the received picture (see Fig. 20a). When the sample is warmed through  $T_c$  and its viscosity increases, precession stops. When normal  $^3\text{He}$  is warmed even further, its viscosity becomes finally so low that precession resumes.

The situation is illustrated schematically in Figs. 21a and 21b. Just above  $T_c$ ,  $^3\text{He}$  is very viscous, like pump oil: when the sample cell with a thin ( $\lesssim 0.5$  mm) layer of normal  $^3\text{He}$  is tilted it takes more than ten minutes before the liquid surface reaches its new equilibrium orientation, perpendicular to gravity. When the tilted cryostat is rotated sufficiently fast, the viscous liquid cannot move quickly enough to keep its surface perpendicular to the gravitation axis  $g$ , which precesses in the coordinate system of the rotating vessel (see Fig. 21a). Instead, the surface profile is determined by the walls of the chamber. No flow of the liquid takes place during rotation, and the light beam reflected from the bottom window of the cell remains unchanged in the coordinate system of the rotating cryostat.

When  $^3\text{He}$  is cooled down to the superfluid state, its viscosity drops suddenly. The surface of the liquid can reach its minimum-energy orientation very fast. When observed from the rotating coordinate system of the tilted cryostat, the surface seems to precess. It remains perpendicular to  $g$  whose relative direction precesses around the axis of the rotating cryostat (see Fig. 21b). Because the light beam is refracted by the  $^3\text{He}$  surface before and after reflection from the bottom window of the cell, the reflected beam precesses in the coordinate system of the optical apparatus, which rotates with the cryostat.

Monitoring the inhomogeneous picture on the video screen, one can see very clearly how the precession of the light beam starts when the sample is cooled through  $T_c$ . This is demonstrated more quantitatively in Fig. 21c, which shows the horizontal position  $\Delta x$  of the circular feature pointed at by the arrow in Fig. 20a as a function of time, when the liquid is cooled from just above  $T_c$  down to about  $0.9T_c$  during a slow rotation. The angular velocity is 30 mrad/s, i.e., 0.3 revolutions per minute. The rotation axis is tilted by  $0.4^\circ$  with respect to gravity. The position of the bright center of the feature was determined from the digitized image by a computer, calculating the center-of-mass of the region inside which the intensity of the pixels was above a certain threshold. When the liquid is in the normal state ( $t < 200$  s) it is so viscous that it follows the walls of the chamber (Fig. 21a) even at a slow rotation velocity, and no precession of the beam is observed. The superfluid transition takes place at  $t \approx 200$  s, and the beam starts to precess at the frequency of rotation. In this experiment the thickness of the sample was less than 0.5 mm. When the layer was about 1-mm thick, precession above  $T_c$  was stopped only when the rotation velocity was above 0.3 rad/s, and with a 6-mm layer the beam was precessing just above  $T_c$  even when the cryostat was rotated at  $\Omega = 1.5$  rad/s.

Fig. 21c shows that the precession of the surface of  $^3\text{He}$  starts very rapidly after the sample has cooled below  $T_c$ . At first sight this may seem somewhat surprising; liquid consists still

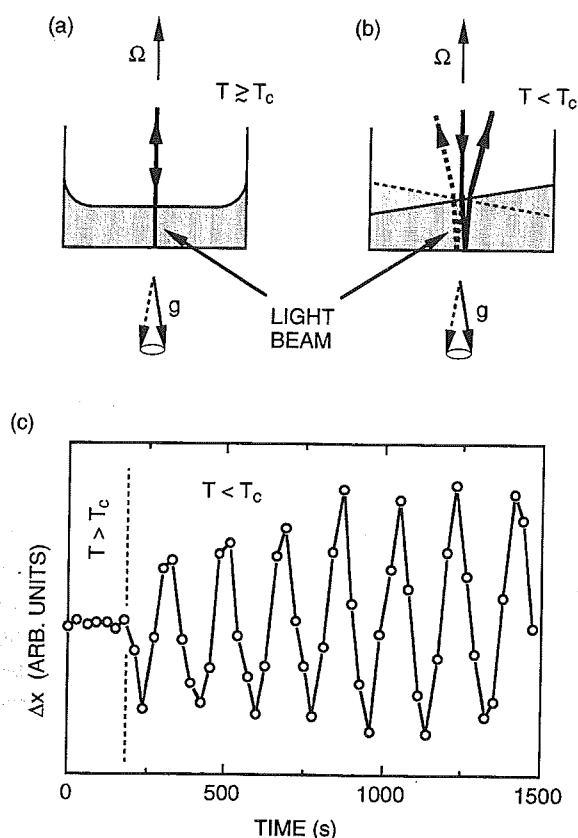


**Figure 21.** Precession of the light beam reflected from the bottom window and refracted by the liquid surface, when the slightly tilted cryostat is rotated. (a) Normal liquid is very viscous at low temperatures and the orientation of its free surface is determined by the walls of the cell; the reflected light beam does not precess. (b) The surface of superfluid  $^3\text{He-B}$  is always perpendicular to gravity and precesses in the coordinate system of the rotating experimental chamber. The reflected light beam precesses as well (thick solid and dotted lines). (c) The horizontal motion of the feature marked by the arrow in Fig. 20a when the cryostat is cooled from the normal into the superfluid state down to  $T \approx 0.9T_c$  while it is continuously rotated at  $\Omega = 0.03$  rad/s. The axis of the cryostat is tilted by  $0.4^\circ$ .

mostly of the very viscous normal component, which cannot move in the direction of the bottom window. However, the normal component can move vertically, and the necessary mass flow in the horizontal direction, required to keep the surface perpendicular to gravity (see Fig. 21c), is performed by the superfluid fraction. Motion of the superfluid component from one part of the chamber to another causes temperature differences within the sample, because there is a one-to-one correspondence between temperature and the relative superfluid density  $\rho_s/\rho$ . However, such temperature gradients are removed by conventional diffusive thermal conductivity with a time constant  $\tau < 0.5$  s.

### 3.2.2. Parabolic surface profile under rotation

When a normal fluid is rotated, its free surface obtains the parabolic profile given by Eq. (7). As Osborne realized in 1950 [15], rotating superfluid  $^4\text{He}$  has the same classical meniscus, showing that the superfluid component rotates with the vessel as well, thus indicating the existence of vortices [16,17]. Later it was confirmed very accurately by optical interferometry [98,99] that the macroscopic surface profile of rotating superfluid  $^4\text{He}$  is given by Eq. (7). In this work, the classical parabolic meniscus and thus the equilibrium number of vortices was observed for rotating superfluid  $^3\text{He-B}$  [P11].

The free surface of a rotating liquid acts as a parabolic mirror, whose focal length  $f$  is

$$f = g/2\Omega^2 \quad (26)$$

for classical liquid or for superfluid with an equilibrium number of vortices (see Eq. (7));  $f = 5$  m when  $\Omega = 1$  rad/s. In the case of a vortex-free superfluid, Eq. (8) gives

$$f = (\rho_n/\rho) g/2\Omega^2. \quad (27)$$

The construction of our optical system is such that at a certain velocity of rotation, all light reflected by the liquid surface focuses onto a single point at the lower end of the optical fiber bundle FB (see Fig. 19) and can be seen as a bright spot on the video screen. Using the dimensions of the setup, taking into account all nonidealities (the incoming beam is not accurately parallel, etc.), focusing is expected to happen when the focal length of the reflecting surface is  $f = 1.1 \pm 0.1$  m. For a classical meniscus, Eq. (26), this corresponds to a rotation velocity  $\Omega_{\text{foc}} = 2.1 \pm 0.1$  rad/s. One should note that this value is based on dimensions measured at room temperature when the cryostat was open. Small changes may take place when the apparatus is closed and cooled down.

As was discussed in Section 3.1.2, most of light that is detected by the CCD camera is reflected from the bottom window WW of the optical cell, while reflection from the liquid surface adds an interference pattern. However, the reflection from the  $^3\text{He}$  sample reaches the video camera only when the free surface of the fluid is approximately parallel to the upper surface of WW, i.e., when WW is normal to gravity: the cryostat has to be slightly tilted, because the reference window is not exactly perpendicular to the axis of the cryostat. When the tilted cryostat is rotated, the interference pattern moves across the screen. The meniscus of the sample reflects light into the fiber bundle FB only during a short fraction of each revolution because of precession of the fluid surface in the coordinate system of the optical apparatus (see Fig. 21b). In our first experiments, the cryostat had to be tilted by  $0.6^\circ$  in order to see the interference pattern. After the sample cell was readjusted at room temperature, the required tilting angle decreased to  $0.1^\circ$ . No difference in focusing was observed between these two cases.

The interference pattern can be seen best when two successive video frames are subtracted from each other (see Fig. 20b). Fig. 22a shows such subtracted pictures from a superfluid sample at  $T/T_c \approx 0.75$ ; similar pictures from normal fluid at  $T \gg T_c$  are presented in Fig. 22b. The interference rings observed when the cryostat was at rest or rotated very slowly are caused by the convex shape of the reference window. The interference pattern becomes smaller when the cryostat is rotated faster, and at  $\Omega = 2.3$  rad/s all light reflected from the

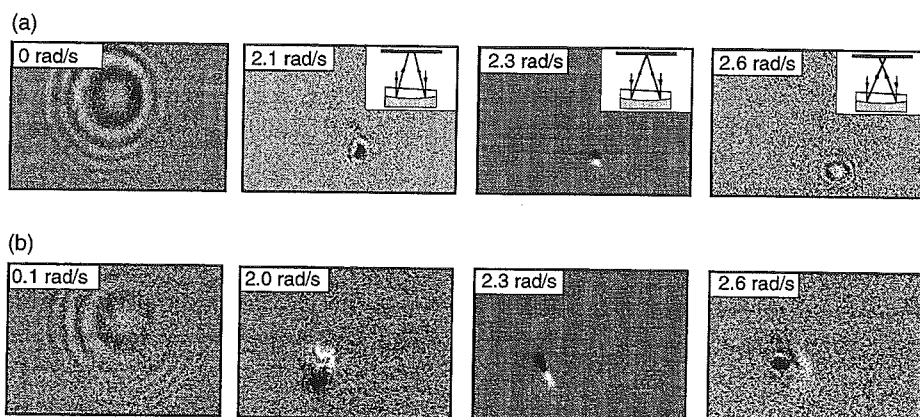


**Figure 22.** Interference patterns produced by light reflected from the bottom window of the sample cell and from the liquid surface for different angular velocities of the cryostat when the sample is (a) in the superfluid state at  $T \approx 0.75T_c$  and (b) in the normal state at  $T \gg T_c$ . The contrast was improved by subtracting two successive video frames (see Fig. 20b). In both cases, light reflected from the liquid surface focuses into one point at  $\Omega \approx 2.3$  rad/s. The insets of the frames in (a) show schematically how focusing takes place.

liquid surface focuses into a single point. The focused reflection is seen as a dark and a bright spot in the frames of Fig. 22; the luminous point moved from one place to another between successive video frames whose difference is shown. Focusing can be seen much better directly on the video monitor than in the printed pictures. When the cryostat is accelerated even more, the focal point moves below the end of the fiber bundle FB, and the size of the observed interference pattern increases again. This process is shown schematically in the insets of Fig. 22a; for clarity, the effect of the lenses L1 and L2 (see Fig. 19a) is not included.

Focusing from the superfluid surface occurred down to the minimum temperature,  $T/T_c = 0.75$ , at the same angular velocity as focusing from the meniscus of the normal liquid, at  $\Omega_{\text{foc}} = 2.25 \pm 0.1$  rad/s. This means that at this velocity the surface of the superfluid had the same macroscopic profile as that of a normal liquid, i.e., that the equilibrium density of vortices was present in the illuminated superfluid region. If there were no vortices, the focusing velocity of the superfluid surface would have been enhanced, according to Eq. (8), with the factor  $(\rho/\rho_n)^{1/2}$ , whose value at  $T/T_c = 0.75$  is 1.17 [100]. The vortex-free superfluid would thus have reflected light into a single point only at  $\Omega = 2.63$  rad/s. The focusing velocity observed is in reasonable agreement with the value  $\Omega_{\text{foc}} = 2.1 \pm 0.1$  rad/s expected for a classical fluid on the basis of the dimensions of the apparatus.

Detection of the equilibrium vortex state is not very surprising in our large cell at  $\Omega = 2.25$  rad/s. For example, in recent NMR-experiments by Parts *et al.* [101], the critical velocity for vortex nucleation in  $^3\text{He-B}$  at  $p = 0$  was less than 5 mm/s. Such a velocity is reached on the side wall of our 20-mm diam cell already at  $\Omega = 0.5$  rad/s. The critical velocity for the nucleation of vortices depends sensitively on the construction of the cell, especially on the

roughness of the walls. No special attention was paid to the smoothness of the copper wall of our experimental cell, so that vortices can possibly form even for  $\Omega \ll 0.5$  rad/s.

The shape of the liquid surface can be determined at any rotation velocity, in principle, from the spacing between the interference fringes. In  $^3\text{He-B}$ , they can be detected even when the sample is several millimeters thick because the viscous normal component keeps the surface quiet. In superfluid  $^4\text{He}$ , the interference pattern is destroyed by vibrations of the liquid surface if the sample is thicker than about  $50\text{ }\mu\text{m}$  [98]. In a conventional interferometer, the thickness of the liquid layer changes between two dark or bright interference rings by exactly one half of the optical wavelength  $\lambda$  in liquid. In our geometry, owing to the focusing effect, the situation is more complicated. Moreover, the shape of our reference window is curved and not known accurately, and the contrast of the interference is not very good.

The aforementioned complications do not prevent a comparison of the interference patterns measured in the superfluid state with those obtained from the normal liquid. However, we cannot, unfortunately, conclude a lot from such comparisons, because the fountain effect changes the free superfluid surface: the superfluid component moves towards the center of the light beam and distorts the surface of the unrotated liquid (see Section 3.2.3). In a sample  $0.5\text{ mm}$  thick, the magnitude of this effect is such that after about  $30\text{ ms}$  of illumination the cryostat must be rotated at  $\Omega \approx 0.3\text{ rad/s}$  to compensate for the convexity of the surface. After the light beam has been switched on for about  $60\text{ ms}$ , so much of the superfluid has accumulated into the center that the surface is flat only when the cryostat is rotated at  $\Omega \approx 0.5\text{ rad/s}$ . At high angular velocities, the fountain effect becomes relatively less important in comparison with the effect of rotation, and it should increase the focusing velocity  $\Omega_{\text{foc}}$  by less than  $0.05\text{ rad/s}$  only.

Another means to study the shape of the free surface at arbitrary  $\Omega$  is to monitor only the light reflected from the reference window WW (see Fig. 19). As discussed in Section 3.2.1, each ray of light is refracted by the liquid surface before and after reflection from WW. When the rotation axis is parallel to the force of gravity, no precession of the light beam occurs. Instead, the beam becomes diverging after it has been refracted twice by the parabolic meniscus of the  $^3\text{He}$ , due to rotation. A measure for the beam expansion can be determined from the positions of inhomogeneities in a similar picture to that shown in Fig. 20a.

The displacement of each inhomogeneity from its location at  $\Omega = 0$  is proportional to  $\Omega^2$ , as expected, and no significant difference between the normal liquid and the superfluid can be detected. However, by measuring the position of only one feature, one cannot unambiguously conclude that the superfluid surface has the same parabolic shape as the surface of the normal liquid and thus the equilibrium density of vortices; the motion can as well be caused by a constant slope of the whole surface, in addition to the parabolic meniscus. In fact, were the center of the experimental chamber not on the rotation axis, the free surface of a rotating vortex-free superfluid would become tilted even at  $T = 0$ , and the slope would be proportional to  $\Omega^2$ . To be sure that the expansion of the beam, caused by the parabolic meniscus, is actually measured, the distance between the two features was determined as a function of  $\Omega$ . Again, no difference between the normal and the superfluid could be observed. Unfortunately, our thermometry was not totally reliable during these experiments, and we can only state that the sample was below  $0.85T_c$ . At such a high temperature, the expected difference in the menisci



of a vortex-free superfluid and a superfluid with equilibrium density of vortices is not larger than the scatter in our data, and the two rotational states cannot be distinguished reliably.

### 3.2.3. Fountain effect

As was mentioned in the previous section, the shape of the superfluid surface changes during illumination: the amount of the liquid in the heated area increases, and the free surface becomes slightly convex. The first three frames in Fig. 23a show the interference patterns obtained from the superfluid at 20-ms intervals under continuous illumination. The contrast was again increased by subtracting two successive video frames from each other (see Fig. 20b). The interference rings shrink towards their center, as can best be seen by following the inner dark ring. Because the reference window WW is convex (see Fig. 23c), this means that

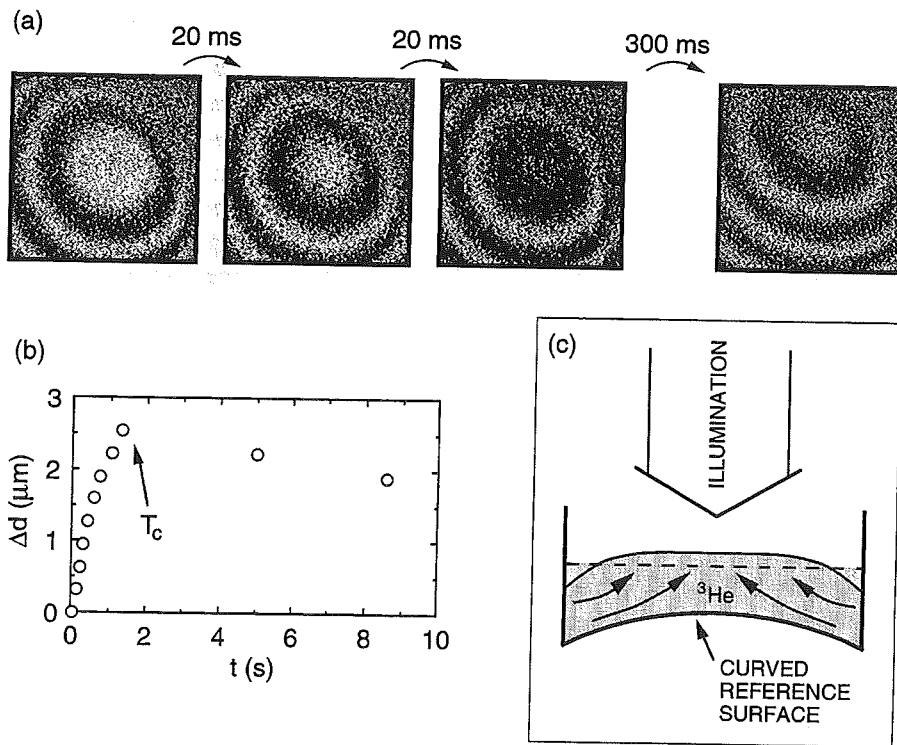


**Figure 23.** (a) Illustration of the fountain effect: the shrinking interference fringes in the superfluid state. The three first frames were taken at 20-ms intervals (from left to right) and the fourth frame 300 ms afterwards. (b) Increase of the sample thickness  $\Delta d$  as a function of time after continuous illumination is started at  $T \approx 0.9T_c$  and the sample warms up to the normal state [P11]. The thickness of the  $^3\text{He}$  layer in the beginning was  $d = 0.5$  mm. (c) A schematic presentation of the fountain effect: the superfluid component flows from the cold perimeter of the cell into the illuminated and warmer center. The superfluid can also enter the optical cell from the filling tube, as explained in text.

the liquid layer thickens. The surface becomes slightly convex during the illumination, but its curvature remains much smaller than that of WW: the spacing between the interference fringes does not change observably. In the center of the rings the surface is parallel with WW, and the distance between the liquid surface and the curved bottom window is at its minimum. In the fourth frame, taken about 300 ms after the first three, the center of the interference pattern has moved towards the upper left corner of the frame, where the filling hole of the cell is located (see Fig. 19b). This means that the surface becomes tilted: the amount of the liquid increases less near the filling tube than far from it.

The change in the thickness  $d$  of the sample can be determined very easily from the interference pattern:  $d$  increases by  $\lambda/2 = 0.316 \mu\text{m}$  each time the center of the fringes changes from bright to dark and to bright again. Fig. 23b is an example of such an experiment. At  $t = 0$ , the illumination of a 0.5-mm thick superfluid sample at  $T \approx 0.9T_c$  is started with a light power of about  $60 \mu\text{W}$ . Within the first 1.2 seconds of illumination, the thickness of the liquid layer increases by about  $2.6 \mu\text{m}$ . At  $t \approx 1.2 \text{ s}$ , the sample has warmed up to the normal state and the surface starts to slowly relax back towards its original position. For a lower initial temperature the thickness of the layer could increase by as much as  $10 \mu\text{m}$  during a few seconds before warming up to  $T_c$ . If the illumination was started above  $T_c$ , no change in the interference pattern was observed.

The most obvious standard explanation for the increased amount of the liquid in the optical cell would be thermal expansion. However, the relative change  $\Delta V/V$  in the volume of  $^3\text{He}$  is only about  $3 \cdot 10^{-7}$  when the sample warms from the minimum temperature  $0.75T_c$  up to  $T_c$  [102]. The total volume of  $^3\text{He}$  in our sample cell and the heat exchanger is about  $25 \text{ cm}^3$ , such that thermal expansion could increase thickness of the  $^3\text{He}$  layer in the chamber of 2-cm diameter not more than  $0.03 \mu\text{m}$ .

Thickening of the liquid layer in the illuminated area can be explained by the fountain effect: light heats the sample locally, and the superfluid component flows from the cold into the warmer regions, tending to decrease differences in temperature. The superfluid flows into the illuminated region probably partly from the perimeter of the cell, as shown schematically in Fig. 23c, and also from the filling tube FT. The normal fraction cannot move away because of its high viscosity, so that the amount of the liquid in the heated area increases. Diffusive heat flow into the heat exchanger area keeps the temperature of the  $^3\text{He}$  near FT lower than far from it. This explains why the liquid surface tilts towards the filling hole (see the last frame in Fig. 23a).

The magnitude of the fountain effect, or the pressure difference  $\Delta p$  caused by a temperature difference  $\Delta T$ , is [2]

$$\Delta p = (S/V)\Delta T, \quad (28)$$

where  $S/V$  is the entropy per unit volume. When  $\Delta p$  corresponds to a difference in the hydrostatic pressure  $\rho gh$  between two parts of the sample, at temperatures  $T$  and  $T + \Delta T$ , respectively, the difference  $\Delta h$  in the thickness of the liquid layer between these two regions is

$$\Delta h = \frac{\Delta p}{\rho g} = \frac{S/V}{\rho g} \Delta T \quad (29)$$

where  $\rho$  is the density of liquid. For  $^3\text{He}$  near  $T_c$ , one obtains  $\Delta h [\mu\text{m}] = 0.73 \Delta T [\mu\text{K}]$ , using for entropy  $S$  its value in the normal Fermi liquid at  $T_c$ ,  $S/n = 0.021 \text{ Jmol}^{-1}\text{K}^{-1}$  [39]. If the superfluid floating from the filling tube FT increases the thickness of the liquid within the sample cell OC by  $10 \mu\text{m}$ , the free surface in FT with a cross-sectional area of  $35 \text{ mm}^2$  lowers by  $90 \mu\text{m}$ , i.e.,  $\Delta h = 100 \mu\text{m}$ . Then the temperature difference between FT and OC is  $\Delta T = \Delta h/0.73 = 140 \mu\text{K}$ . Such a  $\Delta T$  requires a heat flow  $\dot{Q} = \kappa(A/l)\Delta T = 0.05 \mu\text{W}$  through the  $A = 1 \times 1 \text{ mm}^2$  filling hole of length  $l = 0.5 \text{ mm}$ . This is less than 0.1% of the total power of illumination and of the same order of magnitude as the absorption of light into the fused silica window (see Table II). Neither is it totally ruled out that such amount of light could be directly absorbed by the sample. In any case, this simple estimate demonstrates that the fountain effect can increase the thickness of the sample by as much as  $10 \mu\text{m}$ , as experimentally observed.

### 3.3. Future directions

Within conventional two-beam interferometry [103,104] it is quite easy to achieve a depth resolution of  $\lambda/10 \simeq 60 \text{ nm}$ . Such an accuracy may be sufficient for a direct observation of the vortex cluster, which occupies the center of the rotating chamber when the number of vortices is less than in the equilibrium state [105]. Above the cluster the free surface has the classical parabolic meniscus, Eq. (7), while far from it the surface profile of the vortex-free state, Eq. (8), is approached. The vortex cluster can be detected only if the critical velocity for the nucleation of vortices in the optical cell is not too small. When  $\Omega \lesssim 0.2 \text{ rad/s}$ , the surface profiles in the flow states with the equilibrium and nonequilibrium numbers of vortices and in the vortex-free state are too flat to be distinguishable from one another. The interpretation of the interference patterns may be difficult also at higher rotation velocities, owing to the fountain effect.

Marston and Fairbank [106] discovered yet another type of superflow in their optical studies of the free surface of superfluid  $^4\text{He}$ . They were able to create a large superfluid vortex with about 400 circulation quanta in a sample with a thickness of several micrometers. The formation of an analogous giant vortex might be possible in  $^3\text{He-B}$  as well. It would be easily observable by interferometry. Such investigations of the free liquid surface could also be used to detect a new thermal wave, the fifth sound in  $^3\text{He-B}$  [107]. The normal component of the sample is clamped by the bottom of the cell, and a surface wave is produced by the thermal sound mode because of the one-to-one correspondence between temperature and the superfluid density. The fifth sound has been observed in superfluid  $^4\text{He}$  with the use of other techniques [108].

Each vortex in a rotating superfluid is expected to produce a small dimple on the free surface [95,96]. In the case of  $^3\text{He-B}$ , the width of the dimples is about  $50 \mu\text{m}$  but their depth is only about  $1 \text{ nm}$  [P12], owing to the surface tension. Such tiny objects cannot be detected with conventional interferometry. There are more advanced optical techniques available, like phase-contrast microscopy [109] and enhanced phase-shifting interferometry [110], with which the surface profiles could, in principle, be measured even with an accuracy of about  $0.1 \text{ nm}$ . To achieve such accuracies inside the cryostat appears difficult. A further complication

arises from the small reflection coefficient for the free surface of  $^3\text{He}$ :  $R = 1.2 \cdot 10^{-4}$ . Instead of reflection from the liquid surface, one could detect light reflected from the bottom of the cell. However, the change in optical path caused by the dimples is only  $\Delta l = 2d\Delta n \approx 0.04$  nm; here  $d \approx 1$  nm is the depth of the dimple and  $\Delta n = 0.022$  is the difference in the refractive indices of  $^3\text{He}$  [111] and vacuum. One should also keep in mind that the superfluid component rushes into the center of the cell during illumination owing to the fountain effect, and this may cause serious modulations of the vortex dimples.

In the phase-separated  $^3\text{He}$ - $^4\text{He}$  mixture, the surface tension of the boundary between the  $^3\text{He}$ -rich and  $^4\text{He}$ -rich phases is almost an order of magnitude lower than that of the free surface of  $^3\text{He}$ . This increases the size of the defects caused by the vortices. The vortices on the  $^3\text{He}$ -rich phase, which floats on top of the  $^4\text{He}$ -rich phase, cause about 7 nm high bulges onto the boundary [P12]. They are still too small to be observed by conventional interferometry. On the other hand, the vortices on the  $^4\text{He}$ -rich phase produce dimples about 60 nm deep, whose detection by Fizeau interferometry [98] is quite feasible. The positions of the vortices on the  $^3\text{He}$ -rich phase could be determined indirectly, from the distortion which they cause into the incommensurate vortex lattice of  $^4\text{He}$ . In Publication [P12] it is shown with a hydrodynamic calculation that in a separated mixture the vortices on the  $^4\text{He}$ -rich phase have a macrocore filled with  $^3\text{He}$ . A direct experimental observation of the macrocore, whose diameter at low temperatures is only about 1.4 nm, is very difficult. Another prediction of Publication [P12] is that when a dilute solution of  $^3\text{He}$  on  $^4\text{He}$  with a free surface is rotated, a pool filled with  $^3\text{He}$  forms above each vortex before the nucleation of the macrocore.

The boundary between the solid and superfluid phases of  $^3\text{He}$  is another very interesting subject for optical studies. Preliminary experiments have recently been performed in Leiden [112]. Observation of the crystallization waves in  $^3\text{He}$  would be of special interest; such objects have earlier been detected on the boundary between solid and superfluid  $^4\text{He}$  [113].

## 4. Summary

In this thesis, superfluid  $^3\text{He}$  was investigated by phonons and photons, i.e., acoustically and optically. Most of the results on new physical properties of rotating and stationary  $^3\text{He}$ -A and  $^3\text{He}$ -B were obtained with ultrasonic measurements. The principal purpose and the main achievement of the optical experiments was to demonstrate, in practice, the feasibility of optics as a probe of the superfluid phases of  $^3\text{He}$ .

In stationary  $^3\text{He}$ -A, the increase of the ultrasonic attenuation at low temperatures and low pressures was shown to arise from coupling with the re-entrant normal flapping mode near the walls of the experimental chamber, even when the sound velocity is in the direction of a strong magnetic field. The propagation of ultrasound near the mode is nonlinear, i.e., attenuation depends on the size of the sound pulses.

In rotating  $^3\text{He}$ -A, the main outcome of the acoustic experiments was the discovery of a new vortex type, which can exist only in low magnetic fields: a topological first order transition between two continuous vortices was observed when the field was increased from 0 to above 4 mT. Rotating  $^3\text{He}$ -A was studied in high magnetic fields as well, up to about 1 T, but

the interpretation of the data turned out to be more difficult than assumed originally. However, the results support the existence of continuous vortices in all magnetic fields.

Ultrasonic attenuation in stationary and rotating  $^3\text{He-B}$  as a function of the external magnetic field shows anomalous behavior for  $H \approx 200$  mT at pressures below 7 bars. This was interpreted in terms of the distortion of the energy gap. The anisotropic propagation of ultrasound in  $^3\text{He-B}$ , caused by the anisotropy of the energy gap in high magnetic fields, was exploited to study the B-phase under rotation. Evidence was found for the existence of soft vortex cores, in addition to the hard cores. When the sample was cooled from the A- to the B-phase under rotation, a metastable flow state in  $^3\text{He-B}$  was detected, presumably indicating the existence of spin-mass vortices.

The real squashing (rsq) mode, one of the collective modes of the order parameter of  $^3\text{He-B}$ , was studied in magnetic fields below 50 mT. It was shown that all magnetic substates of this mode can couple to ultrasound when the sample is rotated, even when the sound propagates in the direction of the magnetic field.

The real squashing mode could be excited with a nonlinear two-phonon process, by transmitting two sound waves with different frequencies simultaneously through the sample. Two-phonon absorption was applied to study the dispersion relation of the rsq-mode in the absence of a magnetic field, which cannot be realized in linear experiments. Nonlinear acoustic phenomena were also observed near the two-phonon pair-breaking edge, where the combined energy of two phonons is just enough to break a Cooper pair.

In the optical experiments, superfluid  $^3\text{He}$  was *seen* for the first time. The free surface of rotating and stationary  $^3\text{He-B}$  was investigated down to  $T \approx 0.7$  mK. The decrease achieved – by almost two orders of magnitude – in the minimum temperature for optical photography was made possible by new techniques: optical fibers were used to transmit the laser light between room temperature and the cold parts of the cryostat. A drastic decrease in the viscosity of the liquid was seen when the sample was cooled through the superfluid transition under slow rotation. The parabolic meniscus of the rotating liquid was studied by monitoring the light reflected from the liquid surface: the beam focused into a single point at the same angular velocity,  $\Omega_{\text{foc}} = 2.25$  rad/s, both in the normal and in the superfluid states. This means that at this velocity the superfluid macroscopically had the same surface profile as the normal liquid, indicating the presence of an equilibrium number density of vortices. Our technique was not sensitive enough to allow the observation of the dimples that each vortex is predicted to produce on the free surface. The fountain effect in  $^3\text{He-B}$  could be seen as the accumulation of liquid into the illuminated region.

## 5. Publications

- [P1] J.P. Pekola, K. Torizuka, J.M. Kyynäräinen, A.J. Manninen, W. Wojtanowski, and G.K. Tvalashvili, *The Re-entrant Normal Flapping Mode in the Dipolar Boundary Layers of  $^3\text{He-A}$* , Europhys. Lett. **13**, 155 (1990).

The high level of ultrasound attenuation in  $^3\text{He-A}$  at low pressures and low temperatures is shown to arise from the excitation of the re-entrant normal flapping mode, even when sound propagates in the direction of a strong magnetic field. Coupling takes place near the walls, in a boundary layer whose thickness is about the dipolar coherence length  $\xi_d$ . Propagation of ultrasound near the mode is nonlinear, i.e., attenuation depends on the power of the sound pulse.

- [P2] J.P. Pekola, K. Torizuka, A.J. Manninen, J.M. Kyynäräinen, and G.E. Volovik, *Observation of a Topological Transition in the  $^3\text{He-A}$  Vortices*, Phys. Rev. Lett. **65**, 3293 (1990); Erratum, Phys. Rev. Lett. **67**, 1055 (1991).

Rotating  $^3\text{He-A}$  was studied in low magnetic fields, below 20 mT. A topological first-order transition between two continuous vortex textures, dipole-locked and dipole-unlocked, was discovered. The critical field  $H_c$  at which both vortex types have the same free energy was shown to be about 1.5 mT, independent of the rotation velocity. The catastrophe field  $H_{c1}$ , above which dipole-locked low-field vortices cannot exist, is about 4 mT.

- [P3] J.M. Kyynäräinen, J.P. Pekola, A.J. Manninen, and K. Torizuka, *Superfluid  $^3\text{He}$  in Strong Magnetic Fields: Anomalous Sound Attenuation in the B Phase and Evidence for Splitting of the AB Transition*, Phys. Rev. Lett. **64**, 1027 (1990).

Both in stationary and in rotating  $^3\text{He-B}$ , just below the AB transition temperature, anomalous behavior in ultrasonic attenuation versus magnetic field was observed at  $H_c \approx 200$  mT at low pressures. The results were interpreted in terms of distortion of the energy gap: according to the weak-coupling model, the minimum of the gap should transform continuously to zero below  $H_c$  at the AB transition, whereas above  $H_c$  the change should be discontinuous. Increased sound attenuation was detected when the AB phase boundary was moving through the cell. This was suggested to indicate the presence of a new intermediate phase, but it turned out later [P4] that the observation may also be explained by the different sound velocities in  $^3\text{He-A}$  and  $^3\text{He-B}$ .

- [P4] J.M. Kyynäräinen, J.P. Pekola, K. Torizuka, A.J. Manninen, and A.V. Babkin, *Zero-Sound Attenuation in Rotating and Stationary  $^3\text{He-A}$  and  $^3\text{He-B}$* , J. Low Temp. Phys. **82**, 325 (1991).

Acoustic experiments were performed on rotating and stationary  $^3\text{He-A}$  and  $^3\text{He-B}$  in magnetic fields up to 350 mT. The results support the existence of continuous vortices in  $^3\text{He-A}$  and of soft vortex cores in  $^3\text{He-B}$ , but the analysis of the data was not straightforward. The nucleation and decay of vortices was studied. In rotating  $^3\text{He-B}$ , a metastable state was observed after the sample was cooled through the AB transition under rotation. The results of Publication [P3] are discussed in more detail and partially re-interpreted.

- [P5] R.H. Salmelin, J.P. Pekola, A.J. Manninen, K. Torizuka, M.P. Berglund, J.M. Kyynäräinen, O.V. Lounasmaa, G.K. Tvalashvili, O.V. Magradze, E. Varoquaux, O. Avenel, and V.P. Mineev, *Coupling of Zero Sound to the Real Squashing Mode in Rotating  $^3\text{He-B}$* , Phys. Rev. Lett. **63**, 620 (1989).

The first experiments performed in the ROTA2 cryostat are reported. It was found that all five  $m_J$ -states of the real squashing mode in  $^3\text{He-B}$  coupled to ultrasound under rotation in an external magnetic field, even when the sound propagation axis was parallel to the field. Two different rotational states were detected in  $^3\text{He-B}$ . They were interpreted as the vortex-free and the equilibrium vortex states. The textural splitting of the rsq-substate with  $m_J = 0$  was observed, as well as an asymmetry between the heights of the attenuation peaks corresponding to positive and negative  $m_J$ -substates.

- [P6] J.M. Kyynäräinen, A.J. Manninen, K. Torizuka, A.V. Babkin, R.H. Salmelin, G.K. Tvalashvili, and J.P. Pekola, *Ultrasonic Spectroscopy of Rotating  $^3\text{He-B}$* , Zh. Eksp. Teor. Fiz. **98**, 516 (1990) [Sov. Phys. JETP **71**, 287 (1990)].

Experiments on the real squashing mode of  $^3\text{He-B}$  are discussed more thoroughly. The relative strengths of the attenuation maxima corresponding to the different  $m_J$ -substates are in agreement with theory. The gyrosonic effect, i.e., the predicted change in the rsq-spectrum when the relative direction between ultrasound propagation and angular velocity of rotation is reversed, was not observed.

- [P7] K. Torizuka, J.P. Pekola, A.J. Manninen, J.M. Kyynäräinen, and R.H. McKenzie, *Two-Phonon Absorption by the Real Squashing Mode in Superfluid  $^3\text{He-B}$* , Phys. Rev. Lett. **66**, 3152 (1991).

The first experimental observation of a nonlinear parametric acoustic effect on superfluid  $^3\text{He}$  is reported: the real squashing (rsq) mode of  $^3\text{He-B}$  was excited in a two-phonon process. Two parallel sound pulses of different frequencies were simultaneously transmitted through the sample and an attenuation maximum was observed at a the temperature where the sum frequency of the two sound waves was in resonance with the rsq-mode. The height of the peak scaled approximately linearly with the energy of the pump pulse of higher intensity. Even in the absence of a magnetic field a small satellite peak was observed, originating from the reflected pump wave.

- [P8] A.J. Manninen, H. Alles, A.V. Babkin, J.P. Pekola, and R.H. McKenzie, *Observation of Dispersion in the  $J = 2^+$  Collective Modes of  $^3\text{He-B}$  by Nonlinear Acoustic Spectroscopy*, Phys. Rev. Lett. **68**, 3725 (1992).

Two-phonon absorption (TPA) was applied to study the dispersion of the real squashing mode. When the two sound waves were transmitted perpendicular to each other, the dispersion splitting of the rsq-mode could be observed in the absence of a magnetic field: the  $m = 0$  and the  $|m| = 2$  substates coupled to ultrasound at different temperatures. Experimental values for the dispersion coefficients, related to the mode velocities, were extracted from the data. The dispersion relation of the  $m = 0$  submode was studied directly: the mode could be excited at three different wavelengths, keeping its frequency constant.

- [P9] A.J. Manninen, H. Alles, K. Torizuka, A.V. Babkin, and J.P. Pekola, *Experiments on Nonlinear Acoustics in  $^3\text{He-B}$* , Report TKK-F-A713 (1993) [to be submitted to J. Low Temp. Phys.].

A comprehensive summary of our nonlinear acoustic investigations is given. The experiments of Publications [P7] and [P8] are discussed in more detail. Data on the two-phonon absorption observed by transmitting only one energetic single-frequency sound pulse at a time are presented, together with results on the five-fold Zeeman splitting of the TPA-peak. Measurements near the two-phonon pair-breaking edge are described: an anomaly in ultrasound spectra was detected, which split into a triplet when an external magnetic field was applied.

- [P10] A.J. Manninen, H. Alles, A.V. Babkin, and J.P. Pekola, *A Prestudy of Optical Imaging on Superfluid  $^3\text{He}$* , *Physica B* **178**, 352 (1992).

Preliminary results of the experimental feasibility study on optical investigations at ultralow temperatures are reported. Various sources of heat leak into the sample are discussed. The first prototype of a complete system to study the free surface of liquid  $^3\text{He}$  was constructed and tested in a small dilution refrigerator.

- [P11] A.J. Manninen, J.P. Pekola, G.M. Kira, J.P. Ruutu, A.V. Babkin, H. Alles, and O.V. Lounasmaa, *First Optical Observations of Superfluid  $^3\text{He}$* , *Phys. Rev. Lett.* **69**, 2392 (1992).

The first optical experiments on superfluid  $^3\text{He}$  are described. New techniques, based on optical fibers, were employed, which made visual observations possible at temperatures below 1 mK. The drastic change in the viscosity of  $^3\text{He}$  was seen when the sample was cooled through the superfluid transition during rotation. The free surface of rotating  $^3\text{He-B}$  was shown to have the same parabolic meniscus as that in the normal liquid, which implies an equilibrium density of vortices in the superfluid. The fountain effect in  $^3\text{He-B}$  was demonstrated as an accumulation of liquid into the illuminated region.

- [P12] E.B. Sonin and A.J. Manninen, *Downfall of the Vortex Dimple in Superfluids*, *Phys. Rev. Lett.* **70**, 2585 (1993).

The shape of the boundary between the  $^3\text{He}$ -rich and  $^4\text{He}$ -rich phases in the separated  $^3\text{He}$ - $^4\text{He}$  mixture under rotation was studied analytically and numerically, based on a hydrodynamic model. The formation of  $^3\text{He}$ -rich macrocores around the vortices in the  $^4\text{He}$ -rich phase, as a result of an instability on the surface, is discussed. It is also shown that there is a repulsion between the ends of vortices on different sides of the boundary between the two superfluids.



### **The author's contribution:**

All experiments of this thesis were performed as a group effort. I joined the ROTA2 group as a young undergraduate student already in the summer of 1985, when the construction of the cryostat had just started. After the cryostat was manufactured, I was actively involved in finding and repairing the leaks, etc. I also designed and constructed the high-field experimental magnet with the gradient coils, which was used in all acoustical measurements described this thesis, except for those mentioned in Publication [P5]. I have actively participated in the planning, preparing, performing, analysing, and interpreting most of the experiments of this thesis, as well as in operating and maintaining the cryostat. During many of the experiments reported in Publications [P8] and [P9], I concentrated on low-temperature tests of optics, which I carried out principally with J. Pekola. However, I analysed most of the data of Publication [P8] together with H. Alles, and also the previously unpublished results of Publication [P9]. I was the senior graduate student in the ROTA2 group when the experiments described in Publications [P8], [P10] and [P11] were made, and during those measurements of Publication [P9] which were performed in the cubic sound cell. I performed the numerical calculations for Publication [P12]. I have written Publications [P9], [P10], and [P11], and partly Publications [P8] and [P12].

## Acknowledgements

I am deeply grateful to Professor Olli V. Lounasmaa for the privilege of working under his guidance and for his comments on the manuscript of my thesis. The atmosphere and working facilities in his laboratory are really excellent.

I am especially obliged to my supervisor and friend Jukka Pekola. This work would not have been possible without his continuous support. With his own example and everlasting optimism, enthusiasm, and purposefulness he created the wonderful, hard-working but emancipated spirit of the ROTA2 group.

I want to thank P. Berglund, R. Salmelin, and J. Kyynäräinen for constructing a good cryostat and for guidance during my first years in the Low Temperature Laboratory. I am equally grateful to other members of the ROTA2 group, H. Alles, A. Babkin, M. Kira, J. Ruutu, and K. Torizuka, for co-operation and for the good time that we have spent together. Warmest thanks are also due to P. Hakonen who became the new leader of the ROTA2 group after J. Pekola's departure, and to the shorter-time members of our group, O. Andreeva, J.-P. Kneib, O. Jaakkola, M. Laitinen, O. Magradze, L. Mattila, and G. Tvalashvili.

I have benefited from useful discussions with the members of the ROTA1 and YKI groups, A. Annala, J. Ikäheimo, Z. Janú, J. Koivuniemi, Y. Kondo, J. Korhonen, M. Krusius, J. Martikainen, K. Nummila, A. Oja, Ü. Parts, V. Ruutu, J. Tuoriniemi, R. Vuorinen, and W. Yao, and with A. Ahonen, H. Collan, A. Parshin, J. Simola, and B. Ståhlberg. I got very useful advice for optical experiments from M. Kaivola, T. Kajava, P. Kiiveri, H. Ludvigsen, S. Tammela, J. Turunen, and A. Vasara. Much of the electronics for acoustic measurements was kindly provided by O. Avenel and E. Varoquaux.

Discussions with several theoreticians have been extremely valuable for this work. I am especially grateful to R. McKenzie for suggesting us to try to see the two-phonon absorption and for many advice connected with that phenomenon, to G. Volovik for his idea about experimental observation of the topological transition in the A-phase vortices and for important contributions to many other parts of this work as well, to E. Sonin for guiding me with the numerical calculations of Publication [P12], and to M. Salomaa for very useful comments on the manuscript. I am indebted to A. Balatsky, V. Golo, A. Gongadze, B. Kiviladze, G. Kharadze, N. Kopnin, V. Mineev, J. Sauls, P. Soininen, E. Thuneberg, G. Williams, and W. Wojtanowski as well.

I owe much to T. Halme, M. Holmström, T. Koivisto, and L. Pasanen for their help in practical matters, and to M. Hämäläinen for assistance with computers. The skilful staff of the workshop, A. Huvila, J. Kaasinen, S. Kaivola, H. Kaukelin, M. Korhonen, and S. Utriainen, have been of invaluable importance for the success of the experiments of this work. A. Isomäki and A. Salminen are thanked for the reliable delivery of liquid helium. I am indebted to the whole staff of the Low Temperature Laboratory for the nice atmosphere.

Financial support from the Emil Aaltonen foundation is gratefully acknowledged.

Finally, I thank my parents, my sisters Aila and Sanna, and my brother Matti, as well as my other friends and relatives for encouragement and support during these years.

## References

- [1] J. Wilks, *The Properties of Liquid and Solid Helium* (Clarendon Press, Oxford, 1967).
- [2] D.R. Tilley and J. Tilley, *Superfluidity and Superconductivity* (Adam Hilger, Bristol, 1990).
- [3] G. Baym and C. Pethick, *Landau Fermi Liquid Theory* (John Wiley & Sons, New York, 1991).
- [4] J. Bardeen, L.N. Cooper, and J.R. Schrieffer, Phys. Rev. **108**, 1175 (1957).
- [5] D.D. Osheroff, R.C. Richardson, and D.M. Lee, Phys. Rev. Lett. **28**, 885 (1972).
- [6] D. Vollhardt and P. Wölfle, *The Superfluid Phases of Helium 3* (Taylor & Francis, London, 1990).
- [7] G.E. Volovik, *Exotic Properties of Superfluid  $^3\text{He}$*  (World Scientific, Singapore, 1992).
- [8] M.M. Salomaa and G.E. Volovik, Rev. Mod. Phys. **59**, 533 (1987); erratum ibid. **60**, 573 (1988).
- [9] P. Hakonen, O.V. Lounasmaa, and J. Simola, Physica B **160**, 1 (1989).
- [10] P.W. Anderson and P. Morel, Phys. Rev. **123**, 1911 (1961); P.W. Anderson and W.F. Brinkman, Phys. Rev. Lett. **30**, 1108 (1973).
- [11] R. Balian and N.R. Werthamer, Phys. Rev. **131**, 1553 (1963).
- [12] G.A. Kharadze, in *Helium Three*, edited by W.P. Halperin and L.P. Pitaevskii (North-Holland, Amsterdam, 1990), p. 167.
- [13] Y. Kondo, J.S. Korhonen, M. Krusius, V.V. Dmitriev, E.V. Thuneberg, and G.E. Volovik, Phys. Rev. Lett. **68**, 3331 (1992); J.S. Korhonen, Y. Kondo, M. Krusius, E.V. Thuneberg, and G.E. Volovik, submitted to Phys. Rev. B.
- [14] E.M. Lifshitz and L.P. Pitaevskii, *Statistical Physics*, Part 2 (Pergamon, Oxford, 1980).
- [15] D.V. Osborne, Proc. Phys. Soc. London Sect. A **63**, 909 (1950).
- [16] L. Onsager, Nuovo Cimento **6**, Suppl. 2, 249 (1949).
- [17] R.P. Feynman, in *Progress in Low Temperature Physics*, Vol. 1, edited by C.J. Gorter (North-Holland, Amsterdam, 1955), p. 17.
- [18] E.B. Sonin, Rev. Mod. Phys. **59**, 87 (1987).
- [19] G.A. Williams and R.E. Packard, Phys. Rev. Lett. **33**, 280 (1974); G.A. Williams and R.E. Packard, J. Low Temp. Phys. **39**, 553 (1980).
- [20] P.J. Hakonen, O.T. Ikkala, S.T. Islander, O.V. Lounasmaa, T.K. Markkula, P. Roubeau, K.M. Saloheimo, G.E. Volovik, E.L. Andronikashvili, D.I. Garibashvili, and J.S. Tsakadze, Phys. Rev. Lett. **48**, 1838 (1982).
- [21] O.T. Ikkala, G.E. Volovik, P.J. Hakonen, Yu.M. Bun'kov, S.T. Islander, and G.A. Kharadze, Pis'ma Zh. Eksp. Teor. Fiz. **35**, 338 (1982) [JETP Lett. **35**, 416 (1982)].
- [22] A.L. Fetter, in *Progress in Low Temperature Physics*, Vol. 10, edited by D.F. Brewer (North-Holland, Amsterdam, 1986), p. 1.
- [23] M. Krusius, J. Low Temp. Phys., in press (1993).
- [24] N.D. Mermin and T.-L. Ho, Phys. Rev. Lett. **36**, 594 (1976).
- [25] H.K. Seppälä and G.E. Volovik, J. Low Temp. Phys. **51**, 279 (1983).
- [26] P. Hakonen, Ph.D. Thesis, Helsinki University of Technology (1985).
- [27] J.T. Simola, L. Skrbek, K.K. Nummila, and J.S. Korhonen, Phys. Rev. Lett. **58**, 904 (1987).

- [28] E.V. Thuneberg, Phys. Rev. Lett. **56**, 359 (1986); M.M. Salomaa and G.E. Volovik, Phys. Rev. Lett. **56**, 363 (1986).
- [29] Y. Kondo, J.S. Korhonen, M. Krusius, V.V. Dmitriev, Y.M. Mukharsky, E.B. Sonin, and G.E. Volovik, Phys. Rev. Lett. **67**, 81 (1991).
- [30] P.J. Hakonen and K.K. Nummila, Phys. Rev. Lett. **59**, 1006 (1987).
- [31] J.S. Korhonen, A.D. Gongadze, Z. Janú, Y. Kondo, M. Krusius, Yu.M. Mukharsky, and E.V. Thuneberg, Phys. Rev. Lett. **65**, 1211 (1990).
- [32] E.B. Sonin, J. Low Temp. Phys. **55**, 533 (1984).
- [33] K.K. Nummila, P.J. Hakonen, and J.S. Korhonen, Europhys. Lett. **11**, 651 (1990).
- [34] W.F. Brinkman, H. Smith, D.D. Osheroff, and E.I. Blount, Phys. Rev. Lett. **33**, 624 (1974).
- [35] M.M. Salomaa, J. Phys.: Condens. Matter **2**, 1325 (1990).
- [36] L.D. Landau, Zh. Eksp. Teor. Fiz. **32**, 59 (1957) [Sov. Phys. JETP **5**, 101 (1957)].
- [37] B.E. Keen, P.W. Matthews, and J. Wilks, Phys. Lett. **5**, 5 (1963).
- [38] D.T. Lawson, W.J. Gully, S. Goldstein, R.C. Richardson, and D.M. Lee, Phys. Rev. Lett. **30**, 541 (1973).
- [39] W.P. Halperin and E. Varoquaux, in *Helium Three*, edited by W.P. Halperin and L.P. Pitaevskii (North-Holland, Amsterdam, 1990), p. 353.
- [40] Z. Zhao, S. Adenwalla, B.K. Sarma, and J.B. Ketterson, Adv. in Phys. **41**, 147 (1992).
- [41] E.R. Dobbs and J. Saunders, in *Progress in Low Temperature Physics*, Vol. 13, edited by D.F. Brewer (North-Holland, Amsterdam, 1992), p. 91.
- [42] J.W. Serene, Ph.D. Thesis, Cornell University (1974).
- [43] K. Maki, J. Low Temp. Phys. **24**, 755 (1976).
- [44] R.W. Giannetta, A. Ahonen, E. Polturak, J. Saunders, E.K. Zeise, R.C. Richardson, and D.M. Lee, Phys. Rev. Lett. **45**, 262 (1980); D.B. Mast, B.K. Sarma, J.R. Owers-Bradley, I.D. Calder, J.B. Ketterson, and W.P. Halperin, Phys. Rev. Lett. **45**, 266 (1980).
- [45] V.E. Koch and P. Wölfle, Phys. Rev. Lett. **46**, 486 (1981).
- [46] R. Ling, J. Saunders, and E.R. Dobbs, Phys. Rev. Lett. **59**, 461 (1987).
- [47] N. Schopohl and L. Tewordt, J. Low Temp. Phys. **57**, 601 (1984).
- [48] R.H. McKenzie and J.A. Sauls, J. Low Temp. Phys. **90**, 337 (1993).
- [49] L. Tewordt and N. Schopohl, J. Low Temp. Phys. **37**, 421 (1979).
- [50] Yu.A. Vdovin, in *Primenie metodov kvantovoi teorii polya k zadacham mnogikh tel* [Application of the Methods of Quantum Field Theory to Many Body Problems], Proceedings of the Moscow Engineering Physics Institute (Gosatomizdat, Moscow, 1963), p. 65.
- [51] O. Avenel, E. Varoquaux, and H. Ebisawa, Phys. Rev. Lett. **45**, 1952 (1980).
- [52] M.M. Salomaa and G.E. Volovik, J. Low Temp. Phys. **77**, 17 (1989).
- [53] R.S. Fishman and J.A. Sauls, Phys. Rev. B **33**, 6068 (1986).
- [54] B.S. Shivaram, M.W. Meisel, B.K. Sarma, W.P. Halperin, and J.B. Ketterson, Phys. Rev. Lett. **50**, 1070 (1983).
- [55] N. Schopohl, M. Warnke, and L. Tewordt, Phys. Rev. Lett. **50**, 1066 (1983).
- [56] B.S. Shivaram, M.W. Meisel, B.K. Sarma, D.B. Mast, W.P. Halperin, and J.B. Ketterson, Phys. Rev. Lett. **49**, 1646 (1982); see also Ref. [39].

- [57] R.S. Fishman and J.A. Sauls, Phys. Rev. Lett. **61**, 2871 (1988).
- [58] E. Polturak, P.G. deVegvar, E.K. Zeise, and D.M. Lee, Phys. Rev. Lett. **46**, 1588 (1981).
- [59] J.A. Sauls, Phys. Rev. Lett. **47**, 530 (1981); H. Namaizawa, Jpn. J. Appl. Phys. **26**, 165 (1987).
- [60] M. Rouff and E. Varoquaux, Phys. Rev. Lett. **51**, 1107 (1983).
- [61] P.G.N. deVegvar, J. Stat. Phys. **39**, 675 (1985).
- [62] O. Avenel, L. Piché, M. Rouff, E. Varoquaux, R. Combescot, and K. Maki, Phys. Rev. Lett. **54**, 1408 (1985).
- [63] R.H. McKenzie and J.A. Sauls, in *Helium Three*, edited by W.P. Halperin and L.P. Pitaevskii (North-Holland, Amsterdam, 1990), p. 255.
- [64] Y.R. Shen, *The Principles of Nonlinear Optics* (John Wiley & Sons, New York, 1984).
- [65] J.W. Serene, Phys. Rev. B **30**, 5373 (1984).
- [66] R.H. McKenzie and J.A. Sauls, Europhys. Lett. **9**, 459 (1989).
- [67] R.H. McKenzie and J.A. Sauls, Physica B **178**, 219 (1992).
- [68] R.H. Salmelin, J.M. Kyyräinen, M.P. Berglund, and J.P. Pekola, J. Low Temp. Phys. **76**, 83 (1989).
- [69] R. Salmelin, Ph.D. Thesis, Helsinki University of Technology (1989).
- [70] J. Kyyräinen, Ph.D. Thesis, Helsinki University of Technology (1990).
- [71] O.V. Lounasmaa, *Experimental Principles and Methods below 1 K* (Academic Press, London, 1974).
- [72] F. Pobell, *Matter and Methods at Low Temperatures* (Springer-Verlag, Berlin, 1992).
- [73] K. Torizuka, J.P. Pekola, J.M. Kyyräinen, A.J. Manninen, O.V. Lounasmaa, and G.K. Tvalashvili, Physica B **165 & 166**, 623 (1990).
- [74] The transmitter-receiver module was kindly provided by O. Avenel and E. Varoquaux.
- [75] L. Piché, M. Rouff, E. Varoquaux, and O. Avenel, Phys. Rev. Lett. **49**, 744 (1982).
- [76] R. Ling, W. Wojtanowski, J. Saunders, and E.R. Dobbs, J. Low Temp. Phys. **78**, 187 (1990).
- [77] W. Wojtanowski, private communication (1990).
- [78] T. Kopp and P. Wölfe, Phys. Rev. Lett. **59**, 2979 (1987).
- [79] K. Torizuka, Ph.D. Thesis, Helsinki University of Technology (1991).
- [80] K. Torizuka, J.P. Pekola, and A.J. Manninen, Physica B **178**, 244 (1992).
- [81] T. Fujita, M. Nakahara, T. Ohmi, and T. Tsuneto, Prog. Theor. Phys. **60**, 671 (1978).
- [82] P.W. Anderson and G. Toulouse, Phys. Rev. Lett. **38**, 508 (1977); G.E. Volovik and N.B. Kopnin, Pis'ma Zh. Eksp. Teor. Fiz. **25**, 26 (1977) [JETP Lett. **25**, 22 (1977)].
- [83] E.B. Sonin, K. Torizuka, J.M. Kyyräinen, J.P. Pekola, and G.K. Tvalashvili, Phys. Rev. B **45**, 10536 (1992).
- [84] A.J. Manninen, J.M. Kyyräinen, K. Torizuka, and J.P. Pekola, Physica B **165 & 166**, 669 (1990).
- [85] M.M. Salomaa, Nature **326**, 367 (1987).
- [86] M. Ashida and K. Nagai, Prog. Theor. Phys. **74**, 949 (1985).
- [87] G.E. Volovik, Pis'ma Zh. Eksp. Teor. Fiz. **39**, 304 (1984) [JETP Lett. **39**, 365 (1984)].

- [88] J.A. Sauls and J.W. Serene, in *Proceedings of the 17th International Conference on Low Temperature Physics*, edited by U. Eckern, A. Schmid, W. Weber, and H. Wühl (North-Holland, Amsterdam, 1984), p. 775.
- [89] J.P. Pekola, K. Torizuka, A.J. Manninen, H. Alles, and O.V. Lounasmaa, *Physica B* **178**, 238 (1992).
- [90] G.E. Volovik, private communication (1991); Y.R. Shen, private communication (1991).
- [91] P.N. Fraenkel, R. Keolian, and J.D. Reppy, *Phys. Rev. Lett.* **62**, 1126 (1989).
- [92] J.P. Pekola, R.H. Salmelin, A.J. Manninen, K. Torizuka, J.M. Kynnäräinen, and G.K. Tvalashvili, in *Quantum Fluids and Solids – 1989*, AIP Conf. Proc. No. 194, edited by G.G. Ihas and Y. Takano (American Institute of Physics, New York, 1989), p. 63.
- [93] J. Peters and G. Eska, *Europhys. Lett.* **20**, 137 (1992).
- [94] R. Movshovich, N. Kim, and D.M. Lee, *Phys. Rev. Lett.* **64**, 431 (1990).
- [95] H.E. Hall, in *Proceedings of the VIIth International Conference of Low Temperature Physics*, edited by G.M. Graham and A.C. Hollis-Hallett (University of Toronto Press, Toronto, 1961), p. 580.
- [96] K.C. Harvey and A.L. Fetter, *J. Low Temp. Phys.* **11**, 473 (1973).
- [97] P.E. Wolf, F. Gallet, S. Balibar, E. Rolley, and P. Nozières *J. Phys. (Paris)* **46**, 1987 (1985).
- [98] P.L. Marston, Ph.D. Thesis, Stanford University (1976).
- [99] P.L. Marston and W.M. Fairbank, in *Quantum Fluids and Solids*, edited by S.B. Trickey, E.D. Adams, and J.W. Dufty (Plenum, New York, 1977), p. 411.
- [100] J.M. Parpia, D.G. Wildes, J. Saunders, E.K. Zeise, J.D. Reppy, and R.C. Richardson, *J. Low Temp. Phys.* **61**, 337 (1985).
- [101] Ü. Parts, P.I. Soininen, M. Fogelström, Yu.M. Bunkov, V.V. Dmitriev, Y. Kondo, J.S. Korhonen, N.B. Kopnin, and M. Krusius, to be published.
- [102] G.W. Swift and R.E. Packard, *J. Low Temp. Phys.* **43**, 517 (1981).
- [103] M. Born and E. Wolf, *Principles of Optics* (Pergamon Press, Oxford, 1975).
- [104] P. Hariharan, *Optical Interferometry* (Academic Press, Sydney, 1985).
- [105] Y. Kondo, J.S. Korhonen, Ü. Parts, M. Krusius, O.V. Lounasmaa, and A.D. Gongadze, *Physica B* **178**, 90 (1992).
- [106] P.L. Marston and W.M. Fairbank, *Phys. Rev. Lett.* **39**, 1208 (1977).
- [107] G.A. Williams, private communication (1992).
- [108] G.A. Williams, R. Rosenbaum, and I. Rudnick, *Phys. Rev. Lett.* **42**, 1282 (1979); G.J. Jelatis, J.A. Roth, and J.D. Maynard, *Phys. Rev. Lett.* **42**, 1285 (1979).
- [109] A.H. Bennett, H. Jupnick, H. Osterberg, and O.W. Richards, *Phase Microscopy* (John Wiley & Sons, New York, 1951).
- [110] J.C. Wyant and K.N. Prettyjohns, US Patent No. 4,639,139 (1987).
- [111] J. Pipman, S.G. Lipson, J. Landau, and N. Bochner, *J. Low Temp. Phys.* **31**, 119 (1978).
- [112] R. Wagner and G. Frossati, private communication (1993).
- [113] K.O. Keshishev, A. Ya. Parshin, and A.V. Babkin, *Pis'ma Zh. Eksp. Theor. Fiz.* **30**, 63 (1979) [*JETP Lett.* **30**, 56 (1979)].